







RESEARCH ARTICLE

10.1029/2022GC010463

Magnesium and Calcium Isotopic Geochemistry of Silica-Undersaturated Alkaline Basalts: Applications for Tracing Recycled Carbon

Yue Qi¹, Qiang Wang^{1,2} , Gang-Jian Wei^{1,2} , Jie Li^{1,2} , and Derek A. Wyman³ 

¹State Key Laboratory of Isotope Geochemistry, Guangzhou Institute of Geochemistry, Chinese Academy of Sciences, Guangzhou, China, ²CAS Center for Excellence in Deep Earth Science, Guangzhou, China, ³School of Geosciences, The University of Sydney, Sydney, NSW, Australia

Key Points:

- Western Qinling alkaline basalts were derived by partial melting of carbonatite-metasomatized asthenospheric mantle
- The shift in mantle $\delta^{26}\text{Mg}$ values during carbonatite metasomatism depends on the type and amount of carbonatite involved
- The $\delta^{44/40}\text{Ca}$ offset during carbonatite metasomatism depended on the Ca isotope composition of subducted carbonate

Supporting Information:

Supporting Information may be found in the online version of this article.

Correspondence to:

Q. Wang,
wqiang@gig.ac.cn

Citation:

Qi, Y., Wang, Q., Wei, G.-J., Li, J., & Wyman, D. A. (2022). Magnesium and calcium isotopic geochemistry of silica-undersaturated alkaline basalts: Applications for tracing recycled carbon. *Geochemistry, Geophysics, Geosystems*, 23, e2022GC010463. <https://doi.org/10.1029/2022GC010463>

Received 4 APR 2022

Accepted 4 AUG 2022

Abstract Carbon plays important roles in the evolution of the atmosphere and biosphere, and geochemical differentiation in Earth's interior. Most subducted C is recycled to the deep mantle and returns to the surface by degassing from erupted basalts and associated fluids. The Mg–Ca isotopic systems have been widely used in tracing recycled C. However, the idea that these geochemical proxies truly reflect the deep C cycle has been challenged. Here we present whole-rock geochemical and Mg–Ca isotopic compositions of Miocene silica-undersaturated alkaline basalts of the Western Qinling orogen, China. These alkaline basalts are associated with carbonatites and are characterized by low SiO_2 (39.0–43.2 wt.%) and Al_2O_3 (6.98–9.15 wt.%) contents, high $\text{CaO}/\text{Al}_2\text{O}_3$ ratios (1.4–1.8), and positive Nb–Ta and negative Pb–Zr–Hf–Ti anomalies, suggesting they were derived by partial melting of carbonatite-metasomatized asthenospheric mantle. The studied samples have $\delta^{26}\text{Mg}$ values of -0.24‰ to -0.44‰ , ranging from mantle-like values ($\delta^{26}\text{Mg} = -0.25\text{‰} \pm 0.07\text{‰}$) to lower values. This implies that carbonatite metasomatism does not always produce low- $\delta^{26}\text{Mg}$ anomalies. The samples have $\delta^{44/40}\text{Ca}$ values (0.59‰–0.77‰; relative to the standard SRM915a) that are lower than Bulk Silicate Earth ($0.94\text{‰} \pm 0.05\text{‰}$), which are attributed to the involvement of low $\delta^{44/40}\text{Ca}$ recycled carbonate in the mantle source. We suggest that the shift in mantle $\delta^{26}\text{Mg}$ values during carbonatite metasomatism is controlled by the type and amount of carbonatite involved, while Ca isotope variations depend largely on the $\delta^{44/40}\text{Ca}$ values of subducted carbonates. Mg or Ca isotopes alone, however, may not be sufficient to track the deep carbon cycle.

Plain Language Summary Most subducted carbon is retained in the descending slab and recycles to the deep mantle. Mg–Ca isotopes have been used to trace recycled carbon, as sedimentary carbonates have distinctive Mg–Ca isotopic compositions compared to the mantle. In this study, we present whole-rock geochemical and Mg–Ca isotopic compositions of Miocene silica-undersaturated alkaline basalts of the Western Qinling orogen. Results indicate that contribution of recycled carbonates does not always produce low- $\delta^{26}\text{Mg}$ anomalies as previously suggested. Combined with evidence from whole-rock major and trace elements, light $\delta^{44/40}\text{Ca}$ values can be attributed to the involvement of recycled carbonate. However, Ca isotope data alone may not provide sufficient evidence to track recycled carbonate.

1. Introduction

Volatile elements such as carbon (C) play important roles in the evolution of the atmosphere and biosphere as well as influencing the rheological properties of the mantle and geochemical differentiation in the Earth's interior (Dasgupta & Hirschmann, 2010; Luth, 2014; Shirey et al., 2019). Evidence from arc magmatism, ultra-high-pressure metamorphic rocks, and experimental studies suggests that most subducted C is retained in the descending slab and enters the deep mantle (Dasgupta & Hirschmann, 2010; Shirey et al., 2019; Thomson et al., 2016; Wallace, 2005). Experimental studies have shown that the melting of subducted carbonate occurs mainly in the transition zone, producing carbonatite melts (Thomson et al., 2016) that either react with mantle peridotite to form carbonatite-metasomatized peridotites or evolve further to form carbonated silicate melts and alkaline basalts at shallow depths (Dasgupta et al., 2013; Dasgupta & Hirschmann, 2010; Mallik & Dasgupta, 2013, 2014). Therefore, carbonatite, carbonated silicate and alkaline basalt magmas can provide important information on C recycling (Amsellem et al., 2020; Banerjee et al., 2021; Simon, 2022).

© 2022. The Authors.

This is an open access article under the terms of the [Creative Commons Attribution-NonCommercial-NoDerivs License](https://creativecommons.org/licenses/by/4.0/), which permits use and distribution in any medium, provided the original work is properly cited, the use is non-commercial and no modifications or adaptations are made.

Carbon may undergo strong isotopic fractionation during magma degassing, and substitutive geochemical proxies have been developed to elucidate the deep C cycle. For example, lighter $\delta^{26}\text{Mg}$ and $\delta^{44/40}\text{Ca}$ values relative to those of the mantle in mantle-derived mafic rocks have been interpreted as indicating the incorporation of recycled sedimentary carbonates, with marine carbonates having light Mg and Ca isotopic compositions relative to the mantle (Amsellem et al., 2020; Banerjee et al., 2021; Cheng et al., 2018; Huang et al., 2011; Li et al., 2017; Tian et al., 2016). Whether these geochemical proxies accurately reflect the deep C cycle has been challenged. Recent studies suggest that low- $\delta^{26}\text{Mg}$ signatures in basalts may be produced by fractional crystallization of chromite (Su et al., 2019) or variable degrees of partial melting (Zhong et al., 2017). More importantly, carbonatite metasomatism may not produce lighter $\delta^{26}\text{Mg}$ values in mantle peridotite (Su et al., 2019). Subducted silicates may also have low- $\delta^{26}\text{Mg}$ signatures after carbonate-silicate reactions during subduction (Wang et al., 2014; Wang & Li, 2022), resulting in a low- $\delta^{26}\text{Mg}$ mantle source with a low carbonate content (Li et al., 2017; Liu et al., 2022; Wang & Li, 2022). Furthermore, average $\delta^{44/40}\text{Ca}$ values of carbonate sediments are similar to those of Bulk Silicate Earth (BSE) and most mantle peridotites (Blättler & Higgins, 2017). The $\delta^{44/40}\text{Ca}$ values of mantle peridotite affected by carbonatite metasomatism also overlap those of metasomatized silicate-melt mantle peridotite (Ionov et al., 2019; Kang et al., 2017).

Here we focus on Miocene silica-undersaturated alkaline basalts of the Western Qinling orogen, China, which are associated with carbonatites and contain mantle-derived xenoliths (Stoppa & Schiazza, 2013; Su et al., 2010; Yu et al., 2006). We describe major- and trace-element geochemical, and Sr–Nd–Mg–Ca isotopic compositions of these rocks. Results indicate that mantle involving recycled carbonates has normal to low $\delta^{26}\text{Mg}$ values, implying that low- $\delta^{26}\text{Mg}$ anomalies do not constitute evidence for the involvement of recycled carbonate. Although low $\delta^{44/40}\text{Ca}$ values can be attributed to recycled carbonate, Ca isotopes alone may also not provide the “smoking gun” evidence to trace recycled carbonate.

2. Geological Background and Samples

The Qinling Orogenic Belt was formed by collision between the North Qinling Block and South Qinling terrane along the Shangdan suture during the Paleozoic, and collision between the South Qinling terrane and South China Block along the Mianlue suture during the Late Triassic (Dong et al., 2011). The belt is divided into the East and West Qinling areas by the Baoji–Chengdu railway. The Western Qinling orogen (WQO) is bounded by the Songpan–Ganzi terrane to the south along the A'nimaqen–Mianlue suture and the Qilian terrane to the north along the Tangzang–Wushan–Tianshui Fault (Figure 1a; Dong et al., 2011).

Cenozoic alkaline basalt–carbonatite complexes in the WQO are distributed mainly in the south of Lixian County (Figure 1b) and include more than 30 outcrops occurring as volcanic pipes and related tuff rings and sub-volcanic intrusions (Stoppa & Schiazza, 2013; Yu et al., 2006). Individual outcrops usually cover areas of $<1\text{ km}^2$ (Dai et al., 2018; Yu et al., 2006). Phlogopite $^{40}\text{Ar}/^{39}\text{Ar}$ ages and perovskite U–Pb ages of the alkaline basalts suggest that the alkaline basalt–carbonatite complexes were erupted at 23–16 Ma (Liu et al., 2018; Yu et al., 2006). The alkaline basalts are porphyritic and contain phenocrysts of olivine, clinopyroxene, and phlogopite, with the proportions of different phenocrysts varying in individual outcrops. The groundmass comprises mainly clinopyroxene, nepheline, leucite, titanomagnetite, zeolite, perovskite, apatite, phlogopite and melilite. Carbonate globules and ocelli are common in the alkaline basalts (Dai et al., 2018; Stoppa & Schiazza, 2013; Yu et al., 2006). The WQO carbonatites are mainly calcite carbonatites, with some variability in Mg and Fe contents in intrusive facies (Stoppa & Schiazza, 2013; Yu et al., 2006). Mantle-derived xenoliths entrained in these rocks include spinel lherzolite, garnet lherzolite, wehrlite, dunite, websterite and clinopyroxenite, all of which would have originated at depths of 75–120 km (Su et al., 2010, and references therein).

Twenty-one samples of alkaline basalt were collected from five outcrops around Baiguan Village (Figure 1b; Table 1). All samples are porphyritic with phenocrysts of mainly olivine and minor clinopyroxene (Figure 2a). The olivine phenocrysts are subhedral to anhedral and 0.1–1.0 mm in size; clinopyroxene phenocrysts are euhedral and 0.1–2.0 mm in size. The samples contain carbonate ocelli that comprise mainly euhedral–subhedral clinopyroxene. The groundmass consists of clinopyroxene, nepheline, titanomagnetite, zeolite, perovskite, and needle-like apatite, all of which have a uniform distribution (Figure 2b).

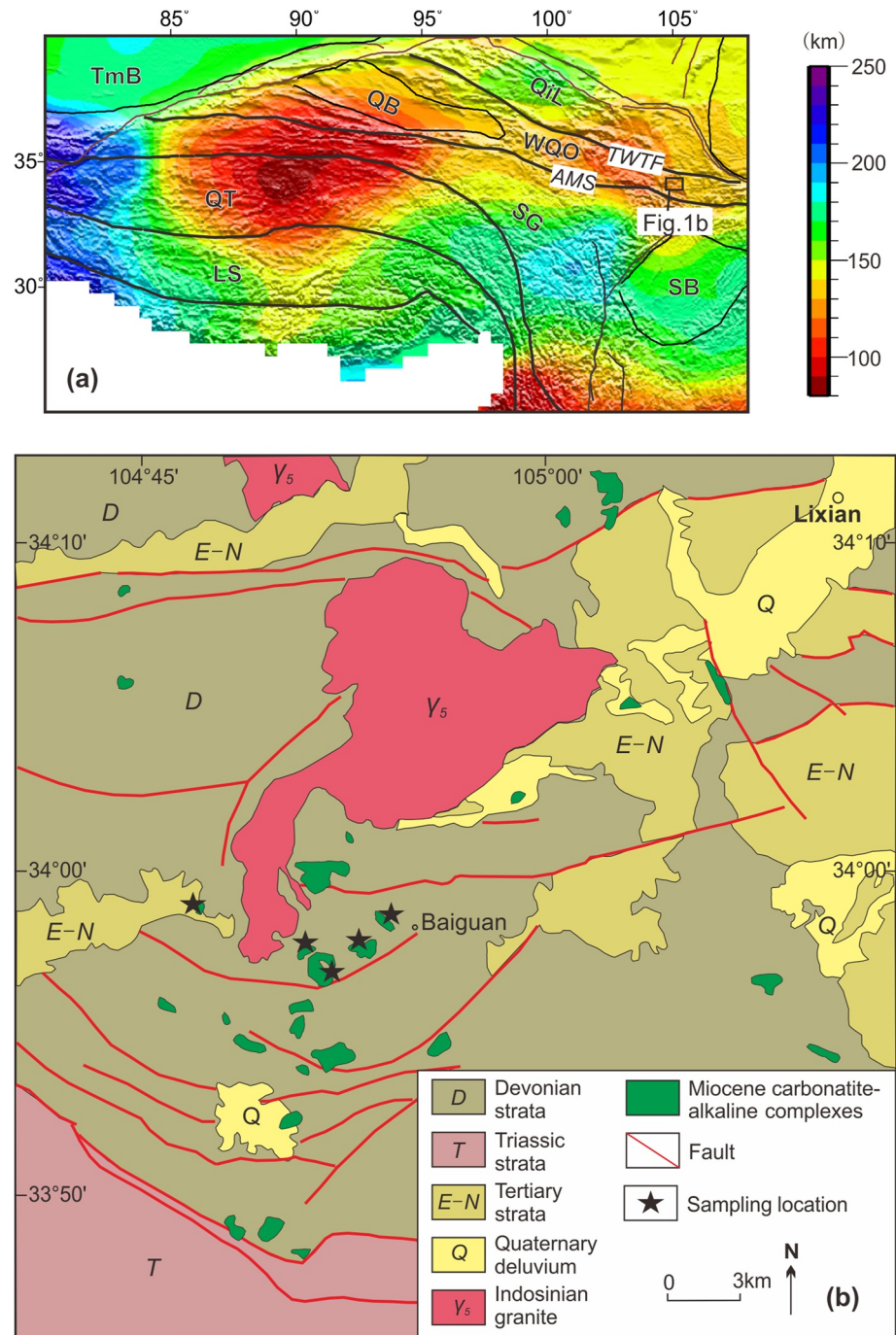


Figure 1. (a) Depth of the thermal lithosphere corresponding to the 1250°C isotherm in and around the Western Qinling orogen (after Deng & Tesauro, 2016). (b) Geological map of the Lixian area (after Yu et al., 2006). LS, Lhasa terrane; QT, Qiangtang terrane; SG, Songpan–Ganzi terrane; WQO, Western Qinling orogen; QB, Qaidam Basin; TmB, Tarim Basin; SB, Sichuan Basin; QiL, Qilian orogeny; AMS, A'nimaqen–Mianlue suture; TWTF, Tangzang–Wushan–Tianshui Fault.

3. Analytical Methods

3.1. Major and Trace Elements

Whole-rock major-element oxide and trace-element compositions were determined at the State Key Laboratory of Isotope Geochemistry, Guangzhou Institute of Geochemistry, Chinese Academy of Sciences (SKLaBIG GIG CAS), by X-ray fluorescence spectroscopy (XRF; RIX 2000, Rigaku, Japan) and inductively coupled plasma–

Table 1
Major and Trace Elements and Sr-Nd Isotopic Compositions

Sample	14WQ01-1	14WQ02-4	14WQ03-1	14WQ03-02	14WQ04	14WQ06	14WQ07
	33°58'44.2"	33°58'44.2"	33°58'44.6"	33°58'44.6"	33°58'44.6"	33°58'44.4"	33°58'44.4"
	104°47'28.8"	104°47'28.8"	104°47'29.3"	104°47'29.3"	104°47'29.3"	104°47'28.8"	104°47'28.8"
SiO ₂	43.2	42.8	42.5	42.9	42.7	42.7	42.5
TiO ₂	3.29	3.19	3.30	3.36	3.24	3.29	3.32
Al ₂ O ₃	9.15	8.91	8.79	9.02	9.09	8.84	8.81
TFe ₂ O ₃	11.8	11.7	11.6	11.7	11.7	11.7	11.8
MnO	0.18	0.18	0.18	0.18	0.19	0.18	0.18
MgO	11.1	11.1	11.2	11.0	10.8	11.0	11.3
CaO	13.1	14.4	14.4	13.6	14.1	14.4	13.8
Na ₂ O	2.30	1.31	0.92	1.80	1.51	1.34	1.15
K ₂ O	2.63	1.64	1.68	2.27	2.02	1.88	2.11
P ₂ O ₅	0.83	0.92	0.85	0.86	0.77	0.84	0.85
LOI	2.38	4.00	3.98	3.00	3.19	3.32	3.87
Total	99.92	100.03	99.34	99.75	99.36	99.57	99.77
CaO/Al ₂ O ₃	1.4	1.6	1.6	1.5	1.6	1.6	1.6
P(GPa)	3.5	3.3	3.4	3.4	3.3	3.4	3.5
T(°C)	1380	1354	1357	1369	1357	1358	1375
Mg [#]	65	65	66	65	65	65	66
K ₂ O/Na ₂ O	1.1	1.3	1.8	1.3	1.3	1.4	1.8
Sc	19.7	19.8	20.0	20.4	20.1	20.0	19.7
V	196	191	197	201	201	196	197
Cr	246	249	255	251	265	246	254
Co	50.5	50.6	51.1	52.4	52.2	51.1	50.8
Ni	205	205	208	212	213	208	206
Cu	93.8	98.8	107	106	106	103	99.8
Zn	138	131	138	142	133	135	132
Ga	17.3	16.9	17.0	17.5	18.0	16.9	16.5
Ge	3.73	3.69	3.81	3.91	3.86	3.79	3.85
Rb	63.8	63.7	59.5	57.3	62.5	58.2	60.7
Sr	1142	1277	1286	1249	1170	1232	1202
Y	25.8	25.9	26.0	26.8	26.6	25.6	25.7
Zr	360	356	362	376	376	360	362
Nb	120	118	120	127	126	121	121
Cs	1.22	2.94	1.44	1.65	1.34	1.39	1.54
Ba	956	1116	948	1024	1019	1046	798
La	76.5	76.2	76.9	78.9	79.4	74.7	77.1
Ce	146	146	147	150	151	143	146
Pr	17.6	17.6	17.8	18.2	18.1	17.3	17.7
Nd	69.0	69.4	69.9	71.3	71.2	68.1	69.5
Sm	12.8	12.9	13.0	13.3	13.2	12.7	13.0
Eu	3.78	3.79	3.81	3.88	3.87	3.73	3.76
Gd	10.5	10.6	10.6	10.8	10.8	10.5	10.6
Tb	1.35	1.36	1.37	1.41	1.38	1.35	1.36

Table 1
Continued

	14WQ01-1	14WQ02-4	14WQ03-1	14WQ03-02	14WQ04	14WQ06	14WQ07
	33°58'44.2"	33°58'44.2"	33°58'44.6"	33°58'44.6"	33°58'44.6"	33°58'44.4"	33°58'44.4"
Sample	104°47'28.8"	104°47'28.8"	104°47'29.3"	104°47'29.3"	104°47'29.3"	104°47'28.8"	104°47'28.8"
Dy	6.53	6.52	6.62	6.66	6.68	6.43	6.50
Ho	1.09	1.10	1.11	1.14	1.12	1.11	1.12
Er	2.46	2.47	2.49	2.56	2.53	2.42	2.46
Tm	0.301	0.299	0.311	0.312	0.314	0.298	0.303
Yb	1.75	1.73	1.77	1.81	1.80	1.76	1.74
Lu	0.239	0.244	0.250	0.251	0.249	0.245	0.245
Hf	8.00	7.76	7.98	8.19	8.12	7.84	7.93
Ta	5.59	5.55	5.63	5.89	5.82	5.65	5.66
Pb	5.26	5.54	6.14	5.45	5.53	6.32	5.38
Th	10.5	10.1	10.6	11.1	11.3	10.5	10.8
U	2.42	2.41	2.43	2.57	2.55	2.38	2.41
Zr/Hf	44.9	45.9	45.4	45.9	46.3	46.0	45.7
La/Yb	44	44	43	44	44	43	44
Dy/Yb	3.7	3.8	3.7	3.7	3.7	3.7	3.7
Hf/Sm	0.62	0.60	0.61	0.61	0.61	0.62	0.61
Nb/U	49.7	49.2	49.4	49.4	49.5	51.0	50.3
Nb/Zr	0.33	0.33	0.33	0.33	0.34	0.34	0.34
⁸⁷ Rb/ ⁸⁶ Sr	0.162			0.133	0.155		0.146
⁸⁷ Sr/ ⁸⁶ Sr	0.704034			0.704014	0.704187		0.704113
2σ	0.000006			0.000007	0.000008		0.000008
(⁸⁷ Sr/ ⁸⁶ Sr) _i	0.70398			0.70397	0.70414		0.70407
¹⁴⁷ Sm/ ¹⁴⁴ Nd	0.1123			0.1129	0.1122		0.1129
¹⁴³ Nd/ ¹⁴⁴ Nd	0.512812			0.512816	0.512819		0.512814
2σ	0.000004			0.000005	0.000004		0.000005
(¹⁴³ Nd/ ¹⁴⁴ Nd) _i	0.512796			0.512800	0.512803		0.512798
ε _{Nd} (22Ma)	3.6			3.7	3.8		3.7
	14WQ14	14WQ15	14WQ15R	14WQ17	14WQ18	14WQ20	14WQ21
	33°57'4.3"	33°57'4.3"	33°57'4.3"	33°57'4.3"	33°57'4.3"	33°58'22.8"	33°58'22.8"
Sample	104°52'9.5"	104°52'9.5"	104°52'9.5"	104°52'9.5"	104°52'9.5"	104°54'15.1"	104°54'15.1"
SiO ₂	39.9	39.9	39.0	40.6	40.5	40.6	41.4
TiO ₂	2.92	3.04	2.90	3.26	3.16	2.88	2.91
Al ₂ O ₃	6.98	7.09	7.28	7.55	7.72	8.08	8.52
TFe ₂ O ₃	11.4	11.3	11.2	11.3	11.1	11.5	11.7
MnO	0.18	0.17	0.17	0.18	0.15	0.17	0.17
MgO	19.7	19.1	19.0	17.1	16.3	13.9	13.3
CaO	12.5	12.7	12.9	13.5	13.0	14.6	14.1
Na ₂ O	0.44	0.40	0.46	1.14	0.86	2.06	1.82
K ₂ O	0.57	0.58	0.61	1.08	0.86	1.58	1.44
P ₂ O ₅	1.28	1.38	1.52	1.15	1.06	0.98	1.03
LOI	3.92	4.00	4.32	2.70	4.67	3.49	3.22

Table 1
Continued

	14WQ14	14WQ15	14WQ15R	14WQ17	14WQ18	14WQ20	14WQ21
	33°57'4.3"	33°57'4.3"	33°57'4.3"	33°57'4.3"	33°57'4.3"	33°58'22.8"	33°58'22.8"
Sample	104°52'9.5"	104°52'9.5"	104°52'9.5"	104°52'9.5"	104°52'9.5"	104°54'15.1"	104°54'15.1"
Total	99.96	99.64	99.42	99.56	99.47	99.79	99.68
CaO/Al ₂ O ₃	1.8	1.8	1.8	1.8	1.7	1.8	1.7
P(GPa)	4.2	4.2	4.0	3.9	3.9	3.6	3.5
T(°C)	1492	1479	1472	1451	1441	1402	1394
Mg [#]	77	77	77	75	74	71	69
K ₂ O/Na ₂ O	1.3	1.5	1.3	0.9	1.0	0.8	0.8
Sc	17.5	18.2	17.4	18.7	17.1	19.8	19.9
V	147	157	150	165	155	185	190
Cr	693	671	666	575	569	434	446
Co	62.1	62.3	60.9	59.1	54.2	56.2	57.1
Ni	539	527	516	461	417	390	396
Cu	75.4	75.5	73.8	72.5	73.0	70.5	66.9
Zn	133	130	131	130	124	128	137
Ga	14.8	15.2	15.0	15.3	14.8	15.3	15.6
Ge	4.07	4.29	4.16	4.31	4.04	3.83	4.04
Rb	17.6	19.4	20.5	31.7	24.9	37.1	35.6
Sr	1488	1760	1579	2314	1333	1018	1033
Y	26.4	27.5	27.9	29.4	26.7	23.6	24.6
Zr	381	393	378	405	394	314	329
Nb	137	142	137	146	134	122	128
Cs	0.364	0.391	0.376	0.304	0.442	0.336	0.374
Ba	942	1057	1254	1680	1388	704	431
La	117	122	119	119	111	90.3	93.9
Ce	223	231	224	224	211	170	175
Pr	26.7	27.3	26.7	26.5	25.1	20.0	20.4
Nd	102	104	102	102	96.0	77.0	78.1
Sm	17.5	18.0	17.7	17.8	16.7	13.5	13.9
Eu	4.83	5.00	4.93	5.05	4.76	3.90	4.00
Gd	13.4	14.0	13.9	14.2	13.0	10.8	11.2
Tb	1.59	1.64	1.62	1.70	1.56	1.32	1.35
Dy	7.19	7.44	7.35	7.76	7.13	6.19	6.38
Ho	1.15	1.21	1.20	1.26	1.16	1.02	1.05
Er	2.45	2.52	2.48	2.68	2.44	2.23	2.32
Tm	0.280	0.291	0.300	0.310	0.292	0.270	0.284
Yb	1.59	1.62	1.63	1.72	1.63	1.54	1.64
Lu	0.206	0.214	0.214	0.233	0.215	0.216	0.223
Hf	7.83	8.26	7.82	8.48	8.23	6.78	6.97
Ta	5.80	5.93	5.82	5.95	5.59	5.47	5.69
Pb	5.73	5.24	4.88	5.22	5.22	3.94	4.41
Th	15.2	15.4	15.0	14.6	14.0	12.0	12.3
U	3.07	3.18	3.10	3.18	2.97	2.51	2.68

Table 1
Continued

	14WQ14	14WQ15	14WQ15R	14WQ17	14WQ18	14WQ20	14WQ21
	33°57'4.3"	33°57'4.3"	33°57'4.3"	33°57'4.3"	33°57'4.3"	33°58'22.8"	33°58'22.8"
Sample	104°52'9.5"	104°52'9.5"	104°52'9.5"	104°52'9.5"	104°52'9.5"	104°54'15.1"	104°54'15.1"
Zr/Hf	48.7	47.5	48.2	47.7	47.9	46.2	47.1
La/Yb	74	75	73	69	68	59	57
Dy/Yb	4.5	4.6	4.5	4.5	4.4	4.0	3.9
Hf/Sm	0.45	0.46	0.44	0.48	0.49	0.50	0.50
Nb/U	44.8	44.5	44.1	45.8	45.0	48.7	47.7
Nb/Zr	0.34	0.36	0.36	0.36	0.36	0.34	0.39
⁸⁷ Rb/ ⁸⁶ Sr	0.034			0.040		0.105	0.100
⁸⁷ Sr/ ⁸⁶ Sr	0.704606			0.705158		0.704388	0.704374
2σ	0.000006			0.000008		0.000009	0.000007
(⁸⁷ Sr/ ⁸⁶ Sr) _i	0.70459			0.70515		0.70435	0.70434
¹⁴⁷ Sm/ ¹⁴⁴ Nd	0.1038			0.1057		0.1056	0.1071
¹⁴³ Nd/ ¹⁴⁴ Nd	0.512813			0.512806		0.512829	0.512817
2σ	0.000004			0.000005		0.000005	0.000005
(¹⁴³ Nd/ ¹⁴⁴ Nd) _i	0.512798			0.512791		0.512813	0.512801
ε _{Nd} (22Ma)	3.7			3.5		4.0	3.7
	14WQ22	S1	S2	S3	S4	S5	14WQ10
	33°58'22.8"	33°57'5.9"	33°57'5.9"	33°57'5.9"	33°57'5.9"	33°57'5.9"	33°57'5.9"
Sample	104°54'15.1"	104°51'3.8"	104°51'3.8"	104°51'3.8"	104°51'3.8"	104°51'3.8"	104°51'3.8"
SiO ₂	40.9	41.0	40.2	40.6	40.7	40.9	40.8
TiO ₂	2.98	3.11	3.12	3.13	3.09	3.18	3.23
Al ₂ O ₃	8.60	7.78	7.44	7.67	7.57	7.63	7.10
TFe ₂ O ₃	11.3	11.5	11.6	11.4	11.6	11.6	12.1
MnO	0.17	0.16	0.16	0.16	0.16	0.16	0.20
MgO	15.7	16.9	17.4	17.3	17.2	17.1	16.6
CaO	13.0	12.8	12.6	12.5	12.8	12.7	12.8
Na ₂ O	1.07	2.46	2.08	2.05	2.20	2.39	2.19
K ₂ O	1.00	1.78	2.74	2.26	2.34	1.73	2.71
P ₂ O ₅	1.03	1.27	1.20	1.07	1.12	1.21	1.04
LOI	3.74	1.40	0.90	1.70	1.31	1.34	0.50
Total	99.56	100.04	99.48	99.85	100.08	99.85	99.32
CaO/Al ₂ O ₃	1.5	1.6	1.7	1.6	1.7	1.7	1.8
P(GPa)	3.6	3.9	4.2	4.1	4.1	4.0	4.3
T(°C)	1429	1466	1499	1487	1484	1471	1493
Mg [#]	73	74	75	75	75	75	73
K ₂ O/Na ₂ O	0.9	0.7	1.3	1.1	1.1	0.7	1.2
Sc	19.1	18.7	19.1	18.3	18.9	18.2	18.9
V	184	161	156	164	162	157	169
Cr	435	629	626	620	602	606	666
Co	55.2	63.6	64.2	62.7	63.7	63.7	64.6
Ni	380	539	545	553	541	548	550

Table 1
Continued

	14WQ22	S1	S2	S3	S4	S5	14WQ10
	33°58'22.8"	33°57'5.9"	33°57'5.9"	33°57'5.9"	33°57'5.9"	33°57'5.9"	33°57'5.9"
Sample	104°54'15.1"	104°51'3.8"	104°51'3.8"	104°51'3.8"	104°51'3.8"	104°51'3.8"	104°51'3.8"
Cu	64.8	161	120	111	117	129	111
Zn	123	142	145	139	139	143	152
Ga	15.6	16.2	15.8	15.9	15.9	16.0	15.7
Ge	3.96	4.19	4.34	4.25	4.37	4.19	4.53
Rb	22.6	49.7	58.0	49.7	53.7	47.7	57.5
Sr	1384	1686	1858	1556	1691	1619	1537
Y	24.0	30.7	31.7	30.6	31.1	29.9	31.1
Zr	318	418	430	426	425	418	436
Nb	123	145	144	141	145	142	146
Cs	0.180	0.583	0.690	0.583	0.702	0.467	0.559
Ba	1207	1070	1384	753	1283	922	926
La	92.3	118	126	119	122	119	124
Ce	172	221	237	223	230	222	233
Pr	20.3	26.2	28.3	26.5	27.3	26.2	27.6
Nd	76.9	101	109	102	105	101	106
Sm	13.6	17.6	19.0	17.9	18.3	17.6	18.8
Eu	3.95	5.02	5.38	5.12	5.17	5.00	5.33
Gd	11.0	14.0	15.0	14.2	14.5	14.0	14.9
Tb	1.35	1.71	1.81	1.74	1.77	1.71	1.83
Dy	6.29	7.78	8.32	8.01	8.12	7.88	8.26
Ho	1.05	1.29	1.36	1.30	1.33	1.28	1.35
Er	2.31	2.76	2.84	2.79	2.81	2.75	2.83
Tm	0.279	0.317	0.334	0.324	0.325	0.321	0.329
Yb	1.63	1.81	1.85	1.82	1.81	1.82	1.86
Lu	0.223	0.240	0.248	0.244	0.245	0.243	0.250
Hf	6.94	8.62	8.96	8.98	8.89	8.81	9.22
Ta	5.61	5.78	6.01	5.80	5.92	5.80	5.99
Pb	4.87	0.564	5.24	1.18	3.96	0.499	2.05
Th	12.1	14.9	16.1	15.1	15.5	15.1	15.8
U	2.48	3.31	3.28	3.27	3.36	3.36	3.44
Zr/Hf	45.8	48.5	48.0	47.4	47.8	47.4	47.2
La/Yb	57	65	68	65	67	65	67
Dy/Yb	3.9	4.3	4.5	4.4	4.5	4.3	4.4
Hf/Sm	0.51	0.49	0.47	0.50	0.49	0.50	0.49
Nb/U	49.7	43.8	43.9	43.2	43.2	42.3	42.5
Nb/Zr	0.39	0.39	0.35	0.33	0.33	0.34	0.34
⁸⁷ Rb/ ⁸⁶ Sr		0.085	0.090	0.092	0.092	0.085	
⁸⁷ Sr/ ⁸⁶ Sr		0.704007	0.703831	0.703823	0.703886	0.704005	
2σ		0.000007	0.000007	0.000008	0.000008	0.000008	
(⁸⁷ Sr/ ⁸⁶ Sr) _i		0.70398	0.70380	0.70379	0.70386	0.70398	
¹⁴⁷ Sm/ ¹⁴⁴ Nd		0.1056	0.1051	0.1061	0.1058	0.1054	

Table 1
Continued

	14WQ22	S1	S2	S3	S4	S5	14WQ10
	33°58'22.8"	33°57'5.9"	33°57'5.9"	33°57'5.9"	33°57'5.9"	33°57'5.9"	33°57'5.9"
Sample	104°54'15.1"	104°51'3.8"	104°51'3.8"	104°51'3.8"	104°51'3.8"	104°51'3.8"	104°51'3.8"
$^{143}\text{Nd}/^{144}\text{Nd}$		0.512810	0.512835	0.512823	0.512834	0.512821	
2σ		0.000005	0.000005	0.000005	0.000005	0.000006	
$(^{143}\text{Nd}/^{144}\text{Nd})_i$		0.512795	0.512820	0.512808	0.512819	0.512806	
$\epsilon_{\text{Nd}}(22\text{Ma})$		3.6	4.1	3.9	4.1	3.8	

Note. $\text{Mg}^\# = \text{Mg}^{2+}/(\text{Mg}^{2+} + \text{Fe}^{2+}) \times 100$; $^{87}\text{Rb}/^{86}\text{Sr}$ and $^{147}\text{Sm}/^{144}\text{Nd}$ are calculated using whole-rock Rb, Sr, Sm and Nd contents; $(^{87}\text{Sr}/^{86}\text{Sr})_i = (^{87}\text{Sr}/^{86}\text{Sr})_s - (^{87}\text{Rb}/^{86}\text{Sr})_s \times (e^{\lambda t} - 1)$, $(^{143}\text{Nd}/^{144}\text{Nd})_i = (^{143}\text{Nd}/^{144}\text{Nd})_{\text{sample}} - (^{147}\text{Sm}/^{144}\text{Nd})_{\text{sample}} \times (e^{\lambda t} - 1)$, $\epsilon_{\text{Nd}}(t) = [(^{143}\text{Nd}/^{144}\text{Nd})_i / (^{143}\text{Nd}/^{144}\text{Nd})_{\text{CHUR}} - 1] \times 10000$, with $t = 22$ Ma in this study. Melting pressures and temperatures were calculated by thermobarometry for CO_2 -rich, silica-undersaturated melts (Sun & Dasgupta, 2020).

mass spectrometry (ICP-MS; Sciex ELAN 6000, Perkin-Elmer, USA), respectively. Analytical uncertainties are 1%–5% for major-element oxides and 3% RSD (relative standard deviation) for most reference-material elements analyzed by ICP-MS. Analytical procedures are described in Li et al. (2002).

3.2. Whole-Rock Sr-Nd Isotopic Compositions

Separation and purification of Sr-Nd isotopes were undertaken at the Key Laboratory of Crust-Mantle Materials and Environments, University of Science and Technology of China (USTC), Hefei, China. Digested samples by HF + HNO_3 were evaporated twice at 130°C–150°C and redissolved in 6 M HCl to remove fluorides. The final residue was dissolved in 1 mL 3M HCl and centrifuged. Sr and rare-earth elements (REEs) were isolated on quartz columns by conventional ion-exchange chromatography with 5 mL Bio Rad AG 50W-X12, 200–400 mesh cation-exchange resin. Nd was separated from REEs on quartz columns containing 1.7 mL Teflon powder coated with HDEHP (di(2-ethylhexyl)orthophosphoric acid) as a cation-exchange medium. Further details are provided by Chen et al. (2000). Sr and Nd isotopic ratios of selected samples were determined using a Micromass Isoprobe multi-collector mass spectrometer (MC-ICP-MS) at SKLaBIG GIG CAS, using procedures similar to those of Li et al. (2004). Measured $^{87}\text{Sr}/^{86}\text{Sr}$ and $^{143}\text{Nd}/^{144}\text{Nd}$ ratios were normalized to $^{86}\text{Sr}/^{88}\text{Sr} = 0.1194$ and $^{146}\text{Nd}/^{144}\text{Nd} = 0.7219$, respectively. Analyses of NBS-SRM 987 and the Shin Etsu JNdi-1 standards during this study yielded average values of $^{87}\text{Sr}/^{86}\text{Sr} = 0.710253 \pm 0.000010$ ($n = 10$; 2SD) and $^{143}\text{Nd}/^{144}\text{Nd} = 0.512109 \pm 0.000003$ ($n = 6$; 2SD).

3.3. Whole-Rock Mg-Ca Isotopic Compositions

Rock powders were digested in concentrated HF– HNO_3 (3:1) in a 7 mL PFA beaker at 110°C for 2–3 days samples, then dried and refluxed with 6 M HCl up to three times until completely dissolved. Sample solutions were divided in half for further separation and purification of Mg-Ca isotopes, respectively. Separation and purification of Mg isotopes were carried out at SKLaBIG GIG-CAS, following the procedure of An et al. (2014). Sample solutions were evaporated to dryness, redigested with aqua regia and dried again before final dissolution in 1 mL 2M HNO_3 for chromatographic separation. Mg separation involved Bio-Rad AG50W-X12 (200–400 mesh) resin. Column chemistry was run in batches of 12 samples, and two reference materials and two blanks were processed with each batch. Total procedural blank was <6 ng Mg, negligible compared to ~50 μg of Mg loaded onto the column. Mg isotopic ratios were determined by Nu Plasma 1700 MC-ICP-MS at SKLaBIG GIG-CAS, using the sample–standard bracketing method. The international standard DSM-3 was measured for bracketing standard, and reference materials BCR-2, BHVO-2, W-2 and GSP-2 and one in-house pure Mg solution standards IGGMg1 were measured for $\delta^{26}\text{Mg}$ values to evaluate analytical quality and reproducibility. The internal precision of measured $^{26}\text{Mg}/^{24}\text{Mg}$ ratios, based on at least three analyses of the same sample solution, was $\leq 0.05\%$ (2SD). The long-term external reproducibility of $^{26}\text{Mg}/^{24}\text{Mg}$ ratios was better than $\pm 0.07\%$ (2SD). Results are reported in standard δ -notation that is defined as $\delta^X\text{Mg} = [(^X\text{Mg}/^{24}\text{Mg})_{\text{sample}} / (^X\text{Mg}/^{24}\text{Mg})_{\text{DSM3}} - 1] \times 1000$, where $X = 25$ or 26.

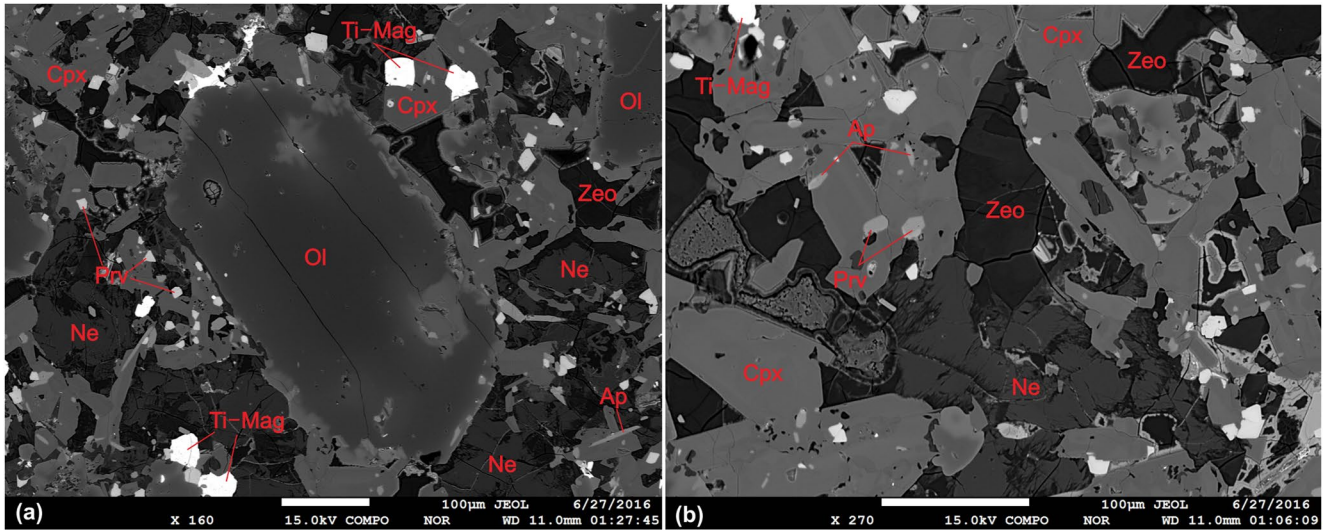


Figure 2. Backscattered-electron images of Miocene alkaline basalts of the Western Qinling orogen. Ol, olivine; Cpx, clinopyroxene; Ne, nepheline; Prv, perovskite; Ti-Mag, titanomagnetite; Ap, apatite; Zeo, zeolite.

Separation and purification of Ca isotopes were also undertaken at SKLaBIG GIG-CAS, following the procedure of Zhu et al. (2016, 2018). Sample solutions were evaporated to dryness before finally dissolution in 1.6 M HCl. An aliquot containing $\sim 50 \mu\text{g}$ Ca was mixed with an appropriate amount of ^{42}Ca - ^{43}Ca double spike solution and the spiked sample solution was loaded onto a Teflon column packed with 1 ml pre-cleaned Bio-Rad AG MP-50 (100–200 mesh) cation-exchange resin. Ca was eluted with 1.6 M HCl with a $>99\%$ Ca yield. The separation procedure was repeated twice to obtain a pure Ca solution. Blanks of the digestion and chemical procedures are $<50 \text{ ng}$, which is insignificant relative to the amount of Ca processed. Calcium isotopic compositions were determined by thermal ionization mass spectrometer (Thermo Triton) at SKLaBIG GIG-CAS. The NIST SRM915a carbonate standard and IAPSO seawater standard IAPSO were analyzed routinely during analytical sessions to monitor instrumental stability. Ca isotopic data are expressed relative to NIST SRM915a and reported as $\delta^{44/40}\text{Ca}$ (‰) = $[(^{44}\text{Ca}/^{40}\text{Ca})_{\text{sample}} / (^{44}\text{Ca}/^{40}\text{Ca})_{\text{NIST SRM 915a}} - 1]$ in this study. The internal precision (reproducibility) of $\delta^{44/40}\text{Ca}$ values was $\pm 0.08\text{‰}$ (2SE) based on triplicate analyses of each sample solution. The 2SD range of average $\delta^{44/40}\text{Ca}$ in SRM915a was $\pm 0.13\text{‰}$ ($n = 61$), representing long-term external precision.

4. Results

4.1. Whole-Rock Major- and Trace-Element Compositions

The alkaline basalt samples have SiO_2 , Al_2O_3 , CaO, and TiO_2 contents of 39.0–43.2, 6.98–9.15, 12.5–14.6, and 2.88–3.36 wt.%, respectively, with CaO/ Al_2O_3 ratios of 1.4–1.8 (Table 1). The samples have variable MgO contents of 10.8–19.7 wt.%, but relatively uniform total Fe_2O_3 contents of 11.1–12.1 wt.% and $\text{Mg}^\#$ values of 65–77. On total-alkali–silica (TAS) diagrams, the rocks plot mainly in the foidite–picrobasalt–basanite field (Figure 3a) with a wide range of $\text{K}_2\text{O}/\text{Na}_2\text{O}$ ratios (0.7–1.9). MgO content is inversely related to Al_2O_3 content (Figure 3b) but has no correlation with total Fe_2O_3 , SiO_2 , CaO, or TiO_2 contents (Figures 3c–3f). All analyzed samples are enriched in light REEs (Figure 4a) with La/Yb and Dy/Yb ratios of 43–75 and 3.7–4.5 (Table 1), respectively. The primitive-mantle-normalized trace element diagram (Figure 4b) indicates enrichment in large-ion lithophile elements, Nb, and Ta, with negative Pb–Zr–Hf–Ti anomalies. Sample Nb/U ratios of 42–51 (Table 1) are similar to those of intraplate oceanic basalts (47 ± 10). The studied samples have $(^{87}\text{Sr}/^{86}\text{Sr})_i$ ratios of 0.7038–0.7051 and $\epsilon_{\text{Nd}}(22\text{Ma})$ values of 3.5–4.1 (Figure 5a). Combining our results with published data (Dai et al., 2017, 2018; Liu et al., 2018; Yu et al., 2006), we observe that high $^{87}\text{Rb}/^{86}\text{Sr}$ ratios (>0.12) samples have a narrow range of $(^{87}\text{Sr}/^{86}\text{Sr})_i$ ratios (0.7038–0.7043), while low $^{87}\text{Rb}/^{86}\text{Sr}$ ratios (<0.12) samples have higher and variable $(^{87}\text{Sr}/^{86}\text{Sr})_i$ ratios (0.7038–0.7059; Figure 5b).

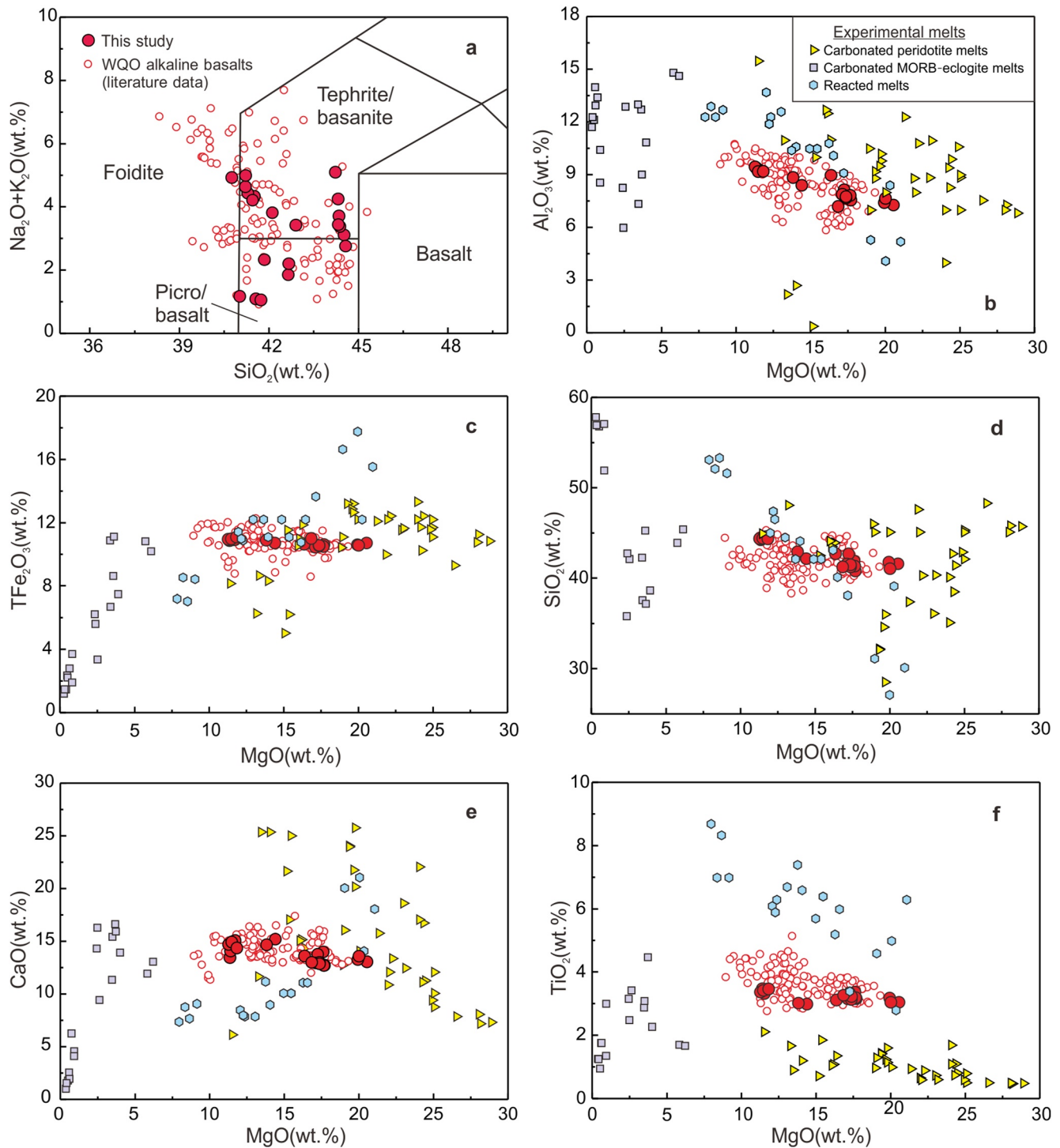


Figure 3. (a) Total-alkali–SiO₂ (TAS) diagram. (b–f) MgO versus Al₂O₃, total Fe₂O₃, SiO₂, CaO, and TiO₂ diagrams. Melts produced by partial melting of carbonated peridotite (Dasgupta et al., 2007, 2013) and carbonated eclogite (Hammouda, 2003; Kiseeva et al., 2012), and by reaction between carbonated eclogite-derived melts and mantle peridotite (Mallik & Dasgupta, 2013, 2014) are shown for comparison. Data for Miocene alkaline basalts of the Western Qinling orogen are from Dai et al. (2017, 2018), Liu et al. (2018) and Yu et al. (2006).

4.2. Whole-Rock Mg–Ca Isotopic Compositions

Magnesium and calcium isotopic compositions of studied samples and standards are reported in Table 2. The $\delta^{26}\text{Mg}$ values of the studied WQO alkaline basalts are between -0.24‰ and -0.44‰ , ranging from mantle-like values ($\delta^{26}\text{Mg} = -0.25\text{‰} \pm 0.07\text{‰}$; Teng, 2017) to lower values (Figure 6). All samples have a narrow range of

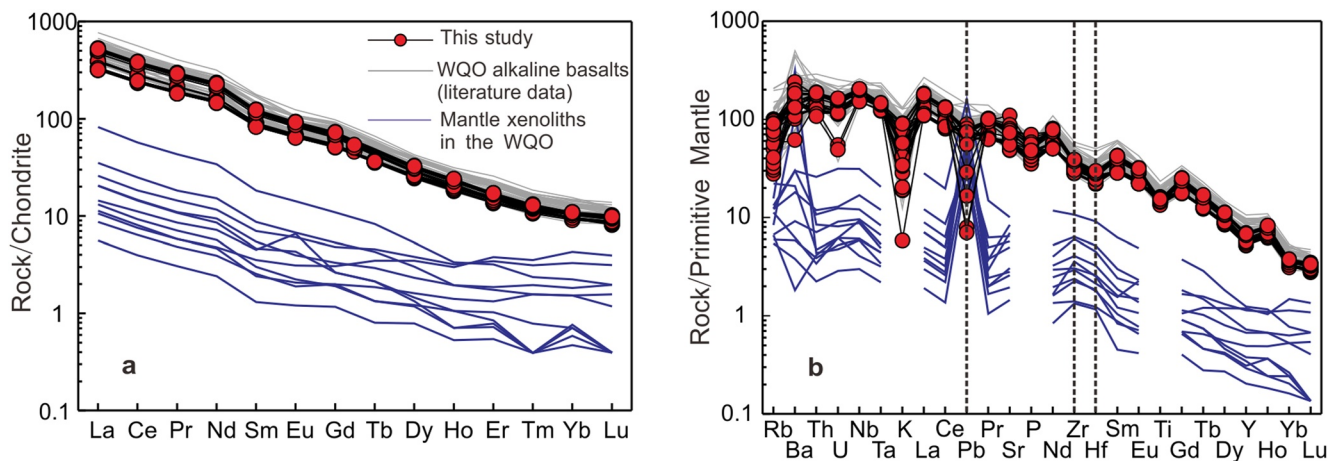


Figure 4. (a) Chondrite-normalized rare-earth element and (b) primitive-mantle-normalized trace-element diagrams for Miocene alkaline basalts of the Western Qinling orogen. Normalizing values are from Sun and McDonough (1989); trace-element compositions of mantle xenoliths are from Su et al. (2012); other data sources are as in Figure 3.

$\delta^{44/40}\text{Ca}$ values (0.63‰–0.77‰; Figure 7a), which are lower than Bulk Silicate Earth (0.94‰ \pm 0.05‰; Kang et al., 2017).

5. Discussion

5.1. Mantle Source of the WQO Alkaline Basalt

Seismic observations have revealed that the lithosphere–asthenosphere boundary beneath the study area is at \sim 120 km depth (Figure 1a; Deng & Tesauro, 2016). Sample melting conditions estimated by thermobarometry for CO_2 -rich, silica-undersaturated melts (Sun & Dasgupta, 2020) are in the range of 1350–1500°C and 3.3–4.3 GPa with an uncertainty of \pm 49°C and \pm 0.5 GPa, respectively (Table 1). Such melting pressures correspond to depths of 105–135 (\pm 20) km [depth (km) = $4.2 + 3.03\text{P}$]. This suggests that the WQO alkaline basalts originated from the base of the lithospheric and/or asthenospheric mantle, although their distinct differences in trace-element and isotopic compositions from those of the lithospheric mantle suggest an asthenospheric origin is more likely. Mantle xenoliths entrained in the WQO alkaline basalts record a wide pressure range of 2.1–3.8 GPa (Su et al., 2010, and references therein), corresponding to depths of 70–120 km. Therefore, the xenoliths provided information on the geochemistry of the lithospheric mantle beneath the study area. They are characterized by posi-

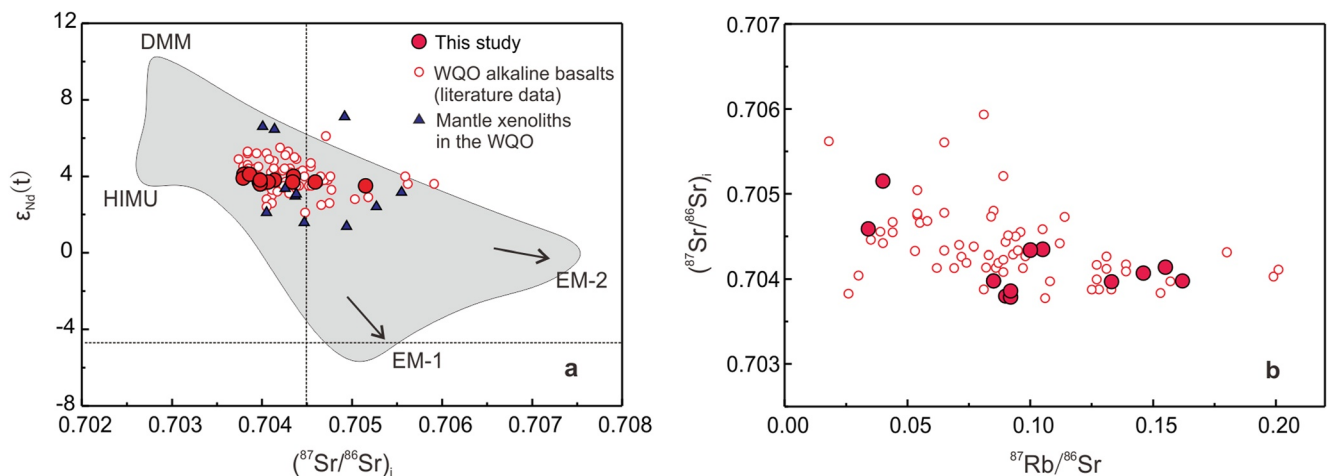


Figure 5. (a) Whole rock Sr–Nd isotopic ratio diagram. (b) $^{87}\text{Rb}/^{86}\text{Sr}$ – $(^{87}\text{Sr}/^{86}\text{Sr})_i$ diagram. Data sources are as in Figure 3.

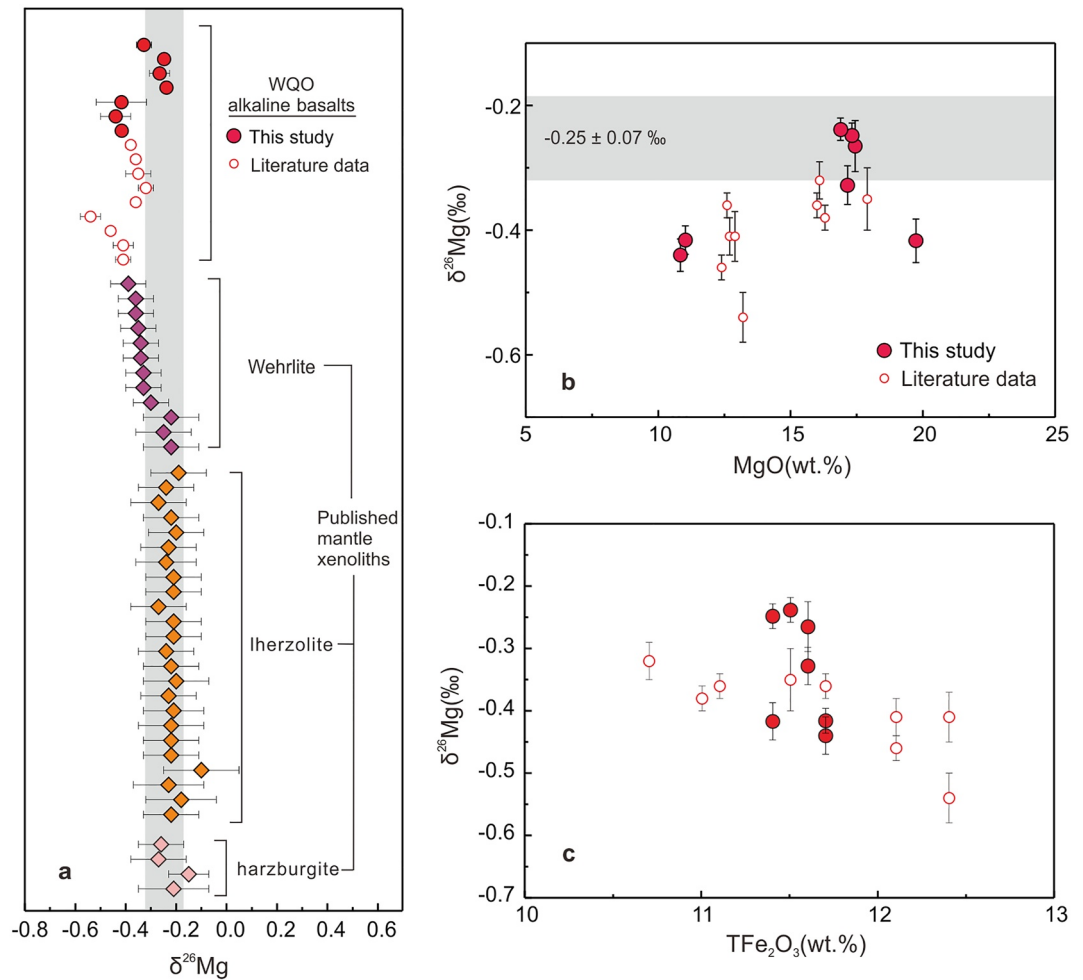


Figure 6. (a) Mg isotopic compositions of carbonatite-metasomatized mantle xenoliths (Su et al., 2019; Xiao et al., 2013) and Miocene alkaline basalts of the Western Qinling orogen (Dai et al., 2017; this study). (b) Plots of MgO content versus $\delta^{26}\text{Mg}$ value. (c) Plots of TFe₂O₃ content versus $\delta^{26}\text{Mg}$ value.

tive Pb–Zr–Hf anomalies (Figure 4b) and high Hf/Sm ratios (0.96–1.8; Su et al., 2012), whereas the WQO alkaline basalts have negative Pb–Zr–Hf anomalies (Figure 4b) and low Hf/Sm ratios (0.39–0.64; Dai et al., 2017, 2018; Lai et al., 2014; Liu et al., 2018; this study). Although the mantle xenoliths and WQO alkaline basalts have similar Sr–Nd isotopic ratios (Figure 5a), they display distinct Pb isotopic compositions with $^{206}\text{Pb}/^{204}\text{Pb}$ ratios of 16.083–18.020 for the mantle xenoliths and 18.088–19.441 for the alkaline basalts (Liu et al., 2018). We therefore conclude that the WQO alkaline basalts were sourced from the asthenospheric mantle.

The WQO alkaline basalts contain mantle-derived xenoliths (Su et al., 2010, 2012) and have high Nb/U ratios (42–51), indicating that they ascended to the surface rapidly without undergoing significant fractional crystallization or crustal contamination. Consequently, their geochemical compositions were inherited from their mantle source. The WQO alkaline basalt samples are strongly enriched in incompatible elements and have enriched Sr–Nd isotopic compositions relative to those of depleted mantle (Figures 4 and 5a), suggesting that their mantle source was metasomatized asthenospheric mantle containing recycled crustal material. The occurrence of associated carbonatites (Dai et al., 2018; Stoppa & Schiazza, 2013; Yu et al., 2006) suggests the involvement of recycled carbonate in the mantle source. The high Zr/Hf (38–65) and low Hf/Sm (0.39–0.64) ratios of the basalt relative to primitive-mantle values of 36 and 0.69, respectively (Sun & McDonough, 1989), also suggest carbonatite metasomatism in the mantle source (Foley et al., 2009; Yaxley et al., 1998).

Experimental studies indicate that carbonatite–alkaline complexes can be derived from direct partial melting of carbonated peridotite or carbonated eclogite (Dasgupta et al., 2007, 2013; Kiseeva et al., 2012), or

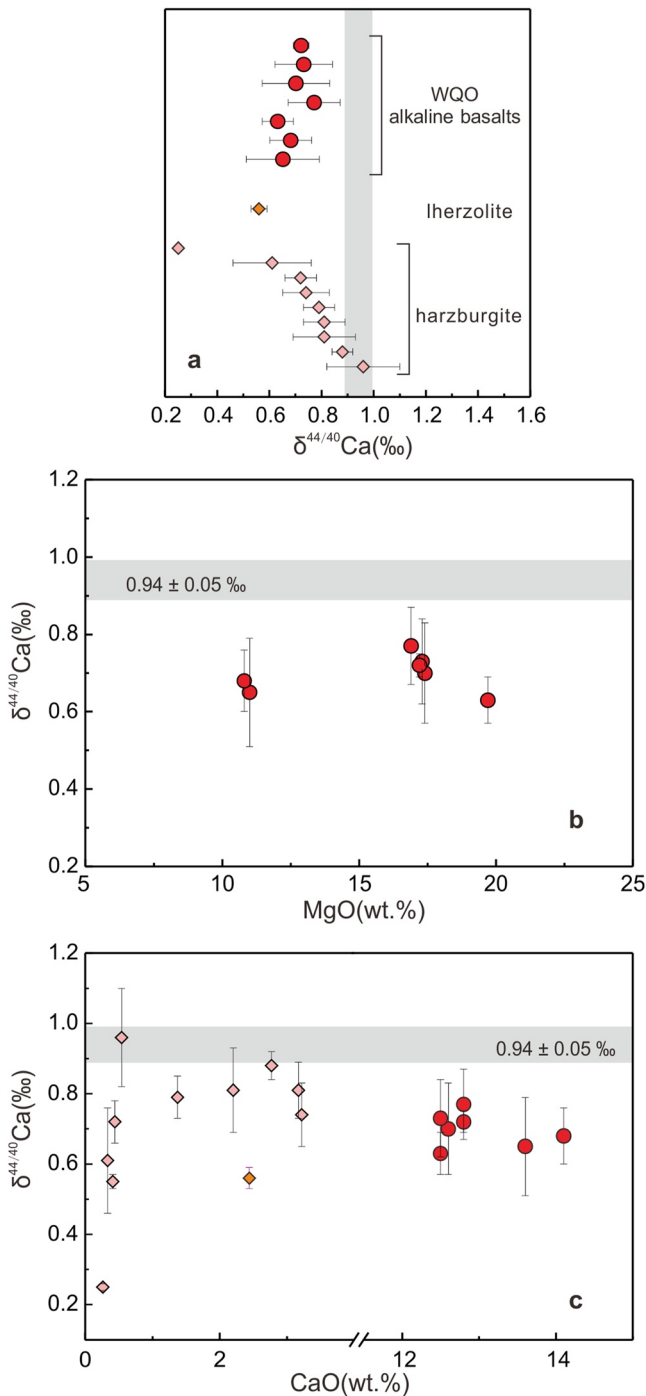


Figure 7. (a) Ca isotopic compositions of carbonatite-metasomatized mantle xenoliths (Ionov et al., 2019; Kang et al., 2017) and Miocene alkaline basalts of the Western Qinling orogen (this study). (b) Plots of MgO content versus $\delta^{44/40}\text{Ca}$ value. (c) Plots of CaO content versus $\delta^{44/40}\text{Ca}$ values for carbonatite-metasomatized mantle xenoliths (Ionov et al., 2019; Kang et al., 2017) and Miocene alkaline basalts of the Western Qinling orogen (this study).

reactions between carbonated eclogite-derived melts and mantle peridotite (Mallik & Dasgupta, 2013, 2014). Melts originating from partial melting of carbonated eclogite generally have low MgO contents (<6.5 wt.%; Hammouda, 2003; Kiseeva et al., 2012), in contrast to the studied samples (>10 wt.%; Figures 3b–3f). Carbonated eclogite-derived melts may acquire high MgO contents after reaction with mantle peridotite, consistent with the systemic co-variation between the MgO and Al_2O_3 , total Fe_2O_3 , SiO_2 , CaO and TiO_2 contents of reacted melts (Mallik & Dasgupta, 2013, 2014). However, the present samples show no such correlations (Figures 3b–3f), further indicating that the WQO alkaline basalts were not produced by reaction between carbonated eclogite-derived melts and mantle peridotite. All samples have relatively low SiO_2 and Al_2O_3 contents, high MgO and CaO contents (Figures 3b–3e), and high CaO/ Al_2O_3 ratios (1.4–1.8), similar to melts derived from partial melting of carbonated peridotite (Dasgupta et al., 2007, 2013). The WQO alkaline basalts have high TiO_2 contents relative to those of experimentally carbonated peridotite-derived melts (Figure 3f), which can be explained by low degree (<5%) partial melting of carbonated peridotite, since the experimental melts were high degree partial melts (Dasgupta et al., 2007). The positive correlation between TiO_2 and total Fe_2O_3 contents (Figure S1a in Supporting Information S1) indicates the suprasolidus breakdown of ilmenite during low-degree partial melting (Foley et al., 2009; Longhi, 1995). We therefore conclude that the WQO alkaline basalts were derived from partial melting of carbonated peridotite.

5.2. Mg–Ca Isotopic Constraints on C Recycling

5.2.1. Heterogeneous Mantle $\delta^{26}\text{Mg}$ Values

The WQO alkaline basalts have variable Mg isotopic compositions ($\delta^{26}\text{Mg} = -0.24$ ‰ to -0.54 ‰ (Figure 6a; Dai et al., 2017; this study), ranging from mantle-like $\delta^{26}\text{Mg}$ values (-0.25 ‰ \pm 0.07‰, Teng, 2017) to subnormal values. Previous studies have suggested that the weathering or surface metasomatic alteration would shift the $\delta^{26}\text{Mg}$ values of basalts (Teng et al., 2010; Wimpenny et al., 2010). Olivine and clinopyroxene are the major Mg-rich minerals in the WQO alkaline basalts, and they are unaltered (Figure 2). In addition, light Mg is preferentially released into fluid during alteration, resulting in heavier Mg isotope compositions in the weathered rocks (Teng et al., 2010; Wimpenny et al., 2010). Hence, the light Mg isotopic compositions of the WQO alkaline basalts would not have been caused by secondary alteration. Additionally, fractional crystallization of chromite and Mg-bearing Fe–Ti oxides may result in $\delta^{26}\text{Mg}$ values decreasing with MgO and total Fe_2O_3 contents (Su et al., 2019; Wang et al., 2021). However, there is no correlation between MgO contents and $\delta^{26}\text{Mg}$ values (Figure 6b) and a negative correlation between total Fe_2O_3 contents and $\delta^{26}\text{Mg}$ values in these alkaline basalts (Figure 6c), which indicates their low and heterogeneous $\delta^{26}\text{Mg}$ values did not result from fractional crystallization.

The occurrence of carbonate globules and ocelli in the groundmass of the WQO alkaline basalts indicates carbonate–silicate immiscibility during magma ascent (Dai et al., 2018). Li et al. (2016) suggested that significant Mg isotopic fractionation can occur during such immiscibility, with

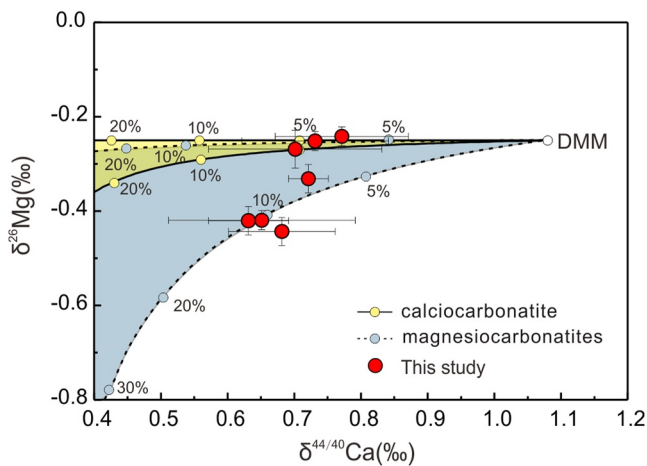


Figure 8. Mg–Ca isotopic binary mixing model of depleted mantle and carbonatites. Solid curves represent the mixing of calciocarbonatite and depleted mantle, and dashed curves the mixing of magnesiocarbonatites and depleted mantle. Calciocarbonatites and magnesiocarbonatites exhibit wide ranges of $\delta^{26}\text{Mg}$ values; the lowest and highest $\delta^{26}\text{Mg}$ values were used in the mixing model. Parameter details are listed in Table 3.

heavy Mg isotopes partitioning preferentially into silicate melts relative to carbonatite melts. Experimental and melt-inclusion studies indicate that carbonate–silicate immiscibility in deep magmas occurs at temperatures of $>1280^\circ\text{C}$ (Panina & Motorina, 2008, and references therein). Theoretical calculations of the Mg isotopic fractionation factor, α , between forsterite and dolomite have yielded $10^3 \ln \alpha_{\text{forsterite-dolomite}}$ values of $<0.10\text{‰}$ at 1280°C (Schauble, 2011). Assuming 0.1‰ Mg fractionation between silicate and carbonatite melts during immiscibility, the $\delta^{26}\text{Mg}$ values of the original melts would be 0.05‰ lighter than those of the analyzed samples after immiscibility. The Mg isotopic fractionation induced by carbonate–silicate immiscibility in the studied samples is thus limited to the level of analytical precision, with the heterogeneous $\delta^{26}\text{Mg}$ values of the alkaline basalts reflecting the Mg isotopic heterogeneity of the magma.

Melting models indicate that low degree partial melting of garnet-bearing peridotite may cause the bulk of residue–melt Mg isotopic fractionation ($<0.1\text{‰}$), since garnet is more enriched in light Mg isotopic compositions (Zhong et al., 2017). However, most Mg would stay in the source residue during partial melting, resulting in limited variation of $\delta^{26}\text{Mg}$ ($<0.02\text{‰}$) in the mantle source (Zhong et al., 2017). Given that the WQO alkaline basalts are derived by partial melting of garnet-phase peridotite, if we assumed maximum 0.1‰ $\delta^{26}\text{Mg}$ difference between the melts and residue, the $\delta^{26}\text{Mg}$ values of mantle sources would be 0.1‰ heavier than those of the analyzed samples (assumed -0.14‰ to -0.44‰). This implies that the heterogeneity in $\delta^{26}\text{Mg}$ values of the WQO alkaline basalts cannot be explained by partial

melting effects but was inherited from the mantle source. The up to $\sim 0.3\text{‰}$ $\delta^{26}\text{Mg}$ offset between the WQO alkaline basalts and terrestrial mantle must reflect the involvement of recycled materials with light Mg isotopic composition.

Field investigations and major- and trace-element compositions of the WQO alkaline basalts lead us to consider that recycled carbonate was directly incorporated into the mantle source. Marine carbonates are the major low- $\delta^{26}\text{Mg}$ reservoirs in recycled crustal materials, with $\delta^{26}\text{Mg}$ values of -5.14‰ to -1.42‰ for calcite-rich carbonates, and -3.25‰ to -0.38‰ for dolomite-rich carbonates (Teng, 2017, and references therein). During subduction, calcite-rich carbonates may not retain their initial Mg isotopic compositions, with $\delta^{26}\text{Mg}$ values shifting toward being isotopically heavier (Wang et al., 2014). In contrast, dolomite-rich carbonates can retain their initial low $\delta^{26}\text{Mg}$ values during subduction (Wang et al., 2014). Considering the distinctive Mg contents and isotopic compositions of Ca-rich and Mg-rich carbonates, the shift in mantle $\delta^{26}\text{Mg}$ values caused by addition of recycled carbonates would depend on the type of carbonates involved (Li et al., 2017; Su et al., 2019). Here, we use Mg isotope compositions of calciocarbonatite and magnesiocarbonatites to represent those of subducted Ca- and Mg-rich carbonates, respectively. A simple binary mixing model for depleted mantle and carbonatites (Figure 8) indicates that recycling of Ca-rich carbonate with mantle-like Mg isotopic compositions would not modify mantle Mg isotopic compositions. Involvement of $>20\%$ Ca-rich carbonate with low $\delta^{26}\text{Mg}$ values (-2.3‰) only can cause $\sim 0.1\text{‰}$ $\delta^{26}\text{Mg}$ offset. Mg-rich carbonates have a wide range of $\delta^{26}\text{Mg}$ values (-3.25‰ to -0.38‰ ; Teng, 2017, and references therein). Recycling of Mg-rich carbonate with high $\delta^{26}\text{Mg}$ values (-0.38‰) also cannot shift the mantle Mg isotopic compositions, while recycling of more than 5% Mg-rich carbonate with extremely low $\delta^{26}\text{Mg}$ values (-3.25‰) would result in 0.1‰ $\delta^{26}\text{Mg}$ offset (Figure 8). Given that carbonatites in the study area are mainly calciocarbonatite with minor magnesiocarbonatites (Stoppa & Schiavizza, 2013; Yu et al., 2006), we argue that the heterogeneous Mg isotopic compositions of the WQO alkaline basalts can be explained by mantle sources with variable mixtures of Ca-rich and Mg-rich carbonates that have different $\delta^{26}\text{Mg}$ values.

5.2.2. Low- $\delta^{44/40}\text{Ca}$ Mantle Sources of the WQO Alkaline Basalts

The WQO alkaline basalts have a narrow Ca isotope compositional range of $\delta^{44/40}\text{Ca} = 0.59\text{‰}$ – 0.77‰ with an average value of $0.70\text{‰} \pm 0.05\text{‰}$ (2SD, $n = 7$) (Table 2), which is lower than the Bulk Silicate Earth (BSE)'s estimated $\delta^{44/40}\text{Ca} = 0.94\text{‰} \pm 0.05\text{‰}$ (2SD; Kang et al., 2017). The lack of a correlation between $\delta^{44/40}\text{Ca}$ values

Table 2
Mg-Ca Isotopes for the Miocene Alkaline Basalts in the Western Qinling Orogeny

Sample	$\delta^{26}\text{Mg}$	2SD	$\delta^{25}\text{Mg}$	2SD	N	$\delta^{44/40}\text{Ca}$	2SD	N
14WQ03-02	-0.416	0.02	-0.185	0.014	3	0.65	0.14	3
Dupl	-0.405	0.02	-0.204	0.076	3	0.59	0.11	3
14WQ04	-0.440	0.03	-0.201	0.029	3	0.68	0.08	3
14WQ14	-0.417	0.03	-0.206	0.022	3	0.63	0.06	3
S1	-0.238	0.02	-0.124	0.044	3	0.77	0.10	3
S2	-0.265	0.04	-0.137	0.016	3	0.70	0.13	3
S3	-0.248	0.02	-0.077	0.041	3	0.73	0.11	3
S4	-0.328	0.03	-0.153	0.007	3	0.72	0.03	3
Standard								
BCR-2	-0.14	0.033	-0.06	0.018	3	0.86	0.09	5
BHVO-2	-0.21	0.039	-0.10	0.019	3			
W-2	-0.21	0.040	-0.11	0.080	3			
GSP-2	0.09	0.040	0.07	0.090	3			
Seawater						1.83	0.12	25
915a						0.01	0.11	38

Note. Dupl = repeat column chemistry and measurement of different aliquots of a stock solution.

& Tipper, 2014; Zhu et al., 2020). Recent studies also show that carbonatites through time have large $\delta^{44/40}\text{Ca}$ variations, ranging from BSE-like to low values (down to $\sim 0.07\%$) (Amsellem et al., 2020; Banerjee et al., 2021; Simon, 2022; Sun et al., 2021). These results indicate that the Ca isotopic compositions of the WQO alkaline basalts may be attributed to the introduction of low $\delta^{44/40}\text{Ca}$ subducted carbonates into their source. Binary mixing results indicate that mantle sources of the WQO alkaline basalts may contain 5%–10% recycled marine carbonates (Figure 8).

Table 3
Detailed Parameters of Mg-Ca Isotopes Binary Mixing Model

	CaO wt%	$\delta^{44/40}\text{Ca}$	MgO wt%	$\delta^{26}\text{Mg}$
Depleted mantle	3.17	1.08	38	-0.25
Magnesiocarbonatites	30	0.26	19	-0.35
	30	0.26	19	-3.25
Calciocarbonatite	50	0.26	0.6	-0.25
	50	0.26	7	-2.3

Note. Depleted mantle: CaO and MgO contents are from Workman and Hart (2005); $\delta^{44/40}\text{Ca}$ values are from Kang et al. (2017) and Ionov et al. (2019), and $\delta^{26}\text{Mg}$ value is from Teng (2017). Magnesiocarbonatites: CaO and MgO contents are from Cheng et al. (2017). $\delta^{44/40}\text{Ca}$ values are from Amsellem et al. (2020). Since Mg-rich carbonates can preserve their initial low $\delta^{26}\text{Mg}$ values during subduction (Wang et al., 2014), we use $\delta^{26}\text{Mg}$ values of Mg-rich carbonates (-3.25% to -0.38%) as the Mg isotopic compositions of magnesiocarbonatites. Calciocarbonatite: CaO and MgO contents are from Ling et al. (2013). $\delta^{44/40}\text{Ca}$ values are from Amsellem et al. (2020) and $\delta^{26}\text{Mg}$ values is from Ling et al. (2013).

and MgO or CaO contents in the WQO alkaline basalts (Figures 7b and 7c) indicates that their low- $\delta^{44/40}\text{Ca}$ signature was not caused by fractional crystallization. As with Mg, Ca isotopic fractionation during carbonate–silicate immiscibility is limited at high temperatures (Amsellem et al., 2020; Banerjee et al., 2021). Recent studies have suggested that Ca-rich carbonate has partitioning similar to clinopyroxene (Wang, Qin, et al., 2017; Wang, Zhou, et al., 2017). Given that clinopyroxene has near-zero equilibrium Ca isotopic fractionation with silicate melt (Chen et al., 2019; Kang et al., 2019), such fractionation between carbonate and silicates melt should also be minor. During mantle melting, light Ca isotopes partition preferentially into melt, and melting models have indicated that $\delta^{44/40}\text{Ca}$ values of melts would be $\sim 0.05\%$ – 0.15% lighter than those of initial peridotite, for varying degrees of melting at 1075–1500°C (Banerjee et al., 2021; Chen et al., 2019). Given that melting temperatures for our samples are 1350–1500°C (Table 1), partial melting can only cause $\sim 0.05\%$ – 0.07% fractionation during partial melting, which is similar to the analytical uncertainty of our $\delta^{44/40}\text{Ca}$ measurements. This implies that the mantle source of the WQO alkaline basalts included recycled materials with light Ca isotopic composition.

Although both recycled carbonates and silicates can decrease mantle Ca isotopic compositions (Ionov et al., 2019), evidence from major-trace elements of the WQO alkaline basalts clearly supports a mantle source including recycled carbonates (see Section 5.1). Marine carbonates have a broad range of Ca isotopic compositions (in excess of 3‰; Fantle & Tipper, 2014), and the average $\delta^{44/40}\text{Ca}$ values of Precambrian marine carbonate sediments are similar to those of BSE (Blättler & Higgins, 2017), while $\delta^{44/40}\text{Ca}$ values of younger (<500 Ma) carbonates are lower than those of BSE values (Fantle & Tipper, 2014; Zhu et al., 2020). Recent studies also show that carbonatites through time have large $\delta^{44/40}\text{Ca}$ variations, ranging from BSE-like to low values (down to $\sim 0.07\%$) (Amsellem et al., 2020; Banerjee et al., 2021; Simon, 2022; Sun et al., 2021). These results indicate that the Ca isotopic compositions of the WQO alkaline basalts may be attributed to the introduction of low $\delta^{44/40}\text{Ca}$ subducted carbonates into their source. Binary mixing results indicate that mantle sources of the WQO alkaline basalts may contain 5%–10% recycled marine carbonates (Figure 8).

Huang et al. (2011) observed a negative correlation between $^{87}\text{Sr}/^{86}\text{Sr}$ ratios and $\delta^{44/40}\text{Ca}$ values in Hawaiian lavas, reflecting the addition of ancient carbonate to the Hawaiian plume. Here, the studied samples have limited $\delta^{44/40}\text{Ca}$ variability and show no evident co-variation with $^{87}\text{Sr}/^{86}\text{Sr}$ ratios (not shown). The low- $^{87}\text{Rb}/^{86}\text{Sr}$ samples of WQO alkaline basalts have higher ($^{87}\text{Sr}/^{86}\text{Sr}$)_i ratios (Figure 4b), suggesting that the ($^{87}\text{Sr}/^{86}\text{Sr}$)_i ratios were inherited from metasomatic agents with high $^{87}\text{Sr}/^{86}\text{Sr}$ ratios and low Rb/Sr ratios rather than from a high-Rb/Sr precursor that developed radiogenic Sr isotopic compositions over time (Pearson et al., 2014). Marine carbonates are characterized by low Rb/Sr ratios (Shields & Veizer, 2002) with mantle-like $^{87}\text{Sr}/^{86}\text{Sr}$ ratios prior to 2.5 Ga and more radiogenic $^{87}\text{Sr}/^{86}\text{Sr}$ ratios later, even exceeding 0.707 during the Phanerozoic (Shields & Veizer, 2002, and references therein). These high $^{87}\text{Sr}/^{86}\text{Sr}$ ratios can be attributed to recycled Phanerozoic carbonates. The Qinling orogen and neighboring areas were affected by subduction during the Silurian–Devonian and Late Triassic (Dong et al., 2011), which may have carried younger carbonates with light Ca isotope compositions to the deep mantle. The light Ca isotopic compositions and high $^{87}\text{Sr}/^{86}\text{Sr}$ ratios accompanying low Rb/Sr ratios may therefore be attributed to recycled carbonates.

5.2.3. Tracing Recycled Carbonates

Carbonatite metasomatism usually results in the conversion of orthopyroxene to clinopyroxene, which in turn may convert refractory harzburgite to lherzolite or wehrlite. The modal mineralogy of metasomatized peridotite depends on the amount of added carbonatite (Yaxley et al., 1998). Yaxley et al. (1998) suggested that harzburgite requires minimal (<2%) or no carbonatite addition, while lherzolite and wehrlite require <8% and 3%–12%, respectively. Given that mantle peridotite has higher MgO content (>35 wt.%) than carbonatite (<20 wt.%), it is inferred that harzburgite may retain mantle Mg isotopic compositions, as the addition of minor carbonatite would not significantly shift mantle $\delta^{26}\text{Mg}$ values. In contrast, for lherzolite and wehrlite the increasing addition of carbonatite may result in lower mantle $\delta^{26}\text{Mg}$ values. Previous studies have reported Mg isotopic compositions for mantle xenoliths (mainly lherzolite and wehrlite, with minor harzburgite) that underwent carbonatite metasomatism (Su et al., 2019; Xiao et al., 2013), with most harzburgite and lherzolite samples having mantle-like Mg isotopic compositions and wehrlite having mantle-like or lighter compositions with $\delta^{26}\text{Mg}$ values as low as to -0.39‰ (Figure 6a). The implication for our samples and mantle xenoliths is that carbonatite metasomatism may induce mantle-like to subnormal $\delta^{26}\text{Mg}$ values (Xiao et al., 2013; Dai et al., 2017; Su et al., 2019; this study), with the shift of mantle $\delta^{26}\text{Mg}$ values by carbonatite metasomatism depending on the type and amount of recycled carbonates involved (Figure 8). Therefore, recycled carbonate does not necessarily induce low- $\delta^{26}\text{Mg}$ anomalies in the mantle (Li et al., 2017; Liu et al., 2022; Wang & Li, 2022).

Unlike the low- $\delta^{26}\text{Mg}$ anomalies of subducted carbonates, the $\delta^{44/40}\text{Ca}$ values of subducted carbonates have heavier, mantle-like to lighter Ca isotope compositions (Blättler & Higgins, 2017; Fantle & Tipper, 2014). Given that the CaO content of mantle (usually <3.5 wt.%) is significantly lower than that of recycled carbonates (30–50 wt.%), any changes in mantle Ca isotope composition depend largely on the $\delta^{44/40}\text{Ca}$ values of subducted carbonates. If the Ca isotope compositions of subducted carbonates are isotopically similar to the BSE, then mantle Ca isotope compositions would not change significantly. Only when isotopically lighter marine carbonates are recycled into the mantle can its Ca isotopic composition potentially decrease. The binary mixing model suggests that addition of ~5% low Ca isotope carbonatite (~0.26‰) can generate the 0.3‰ $\delta^{44/40}\text{Ca}$ offset (Figure 8). Prior studies have shown that carbonatite-metasomatized mantle xenoliths have large $\delta^{44/40}\text{Ca}$ variations of 0.25‰–0.96‰, ranging from BSE-like to low $\delta^{44/40}\text{Ca}$ values (Figure 7; Ionov et al., 2019; Kang et al., 2017). This range overlaps the compositions of our studied WQO alkaline basalts (0.70‰ \pm 0.05‰) and published carbonatites (0.44‰–1.05‰: Banerjee et al., 2021; Sun et al., 2021; Simon, 2022; 0.26‰ \pm 0.25‰: Amsellem et al., 2020). Hence, carbonatite-metasomatism also results in locally heterogeneous Ca isotopic compositions in the mantle, and the variations of mantle Ca isotopic composition depended on the Ca isotopic compositions of subducted carbonates.

6. Conclusions

Based on field investigations, major- and trace-element compositions, and Sr–Nd–Mg–Ca isotopic compositions of Miocene silica-undersaturated alkaline basalts in the western Qinling orogenic belt, we arrived at the following conclusions.

1. The alkaline basalts were derived from partial melting of carbonatite-metasomatized asthenospheric mantle.
2. The basalts have mantle-like to subnormal $\delta^{26}\text{Mg}$ values (-0.24‰ to -0.54‰), and the nature of the shift in mantle $\delta^{26}\text{Mg}$ values during carbonatite metasomatism depends on the type and amount of carbonatite.
3. The basalts have light Ca isotopic compositions ($\delta^{44/40}\text{Ca} = 0.59\text{‰}$ – 0.77‰), that reflect the involvement of low $\delta^{44/40}\text{Ca}$ recycled carbonate. The $\delta^{44/40}\text{Ca}$ offset during carbonatite metasomatism depended on the Ca isotope composition of subducted carbonate.
4. Globally, Mg and Ca isotope data alone may not provide sufficient evidence to track recycled carbonate in the mantle.

Data Availability Statement

The data used in this study can be obtained from the EarthChem Library (<https://doi.org/10.26022/IEDA/112514>).

Acknowledgments

The Editor Professor Paul D. Asimow, Professor Justin I. Simon, and an anonymous reviewer are acknowledged for their reviews on the manuscript. We thank Zhaofeng Zhang, Hongli Zhu, Yajun An and Xiang-Lin Tu for their assistance with whole rocks geochemical compositions and Mg-Ca isotope analyses. Financial support for this research was provided by the National Natural Science Foundation of China (91855215 and 42021002), the Second Tibetan Plateau Scientific Expedition and Research (STEP) (2019QZKK0702), Strategic Priority Research Program (A) of the Chinese Academy of Sciences (CAS; XDA2007030402), and Director's Fund of Guangzhou Institute of Geochemistry, CAS (2020000173). This is contribution No. IS-3231 from GIGCAS.

References

Amsellem, E., Moynier, F., Bertrand, H., Bouyon, A., Mata, J., Tappe, S., & Day, J. M. D. (2020). Calcium isotopic evidence for the mantle sources of carbonatites. *Science Advances*, 6(23), 6. <https://doi.org/10.1126/sciadv.aba3269>

An, Y. J., Wu, F., Xiang, Y. X., Nan, X. Y., Yu, X., Yang, J. H., et al. (2014). High-precision Mg isotope analyses of low-Mg rocks by MC-ICP-MS. *Chemical Geology*, 390, 9–21. <https://doi.org/10.1016/j.chemgeo.2014.09.014>

Banerjee, A., Chakrabarti, R., & Simonetti, A. (2021). Temporal evolution of 644/40Ca and ⁸⁷Sr/⁸⁶Sr of carbonatites: Implications for crustal recycling through time. *Geochimica et Cosmochimica Acta*, 307, 168–191. <https://doi.org/10.1016/j.gca.2021.05.046>

Blättler, C. L., & Higgins, J. A. (2017). Testing Urey's carbonate-silicate cycle using the calcium isotopic composition of sedimentary carbonates. *Earth and Planetary Science Letters*, 479, 241–251. <https://doi.org/10.1016/j.epsl.2017.09.033>

Chen, C., Dai, W., Wang, Z., Liu, Y., Li, M., Becker, H., & Foley, S. F. (2019). Calcium isotope fractionation during magmatic processes in the upper mantle. *Geochimica et Cosmochimica Acta*, 249, 121–137. <https://doi.org/10.1016/j.gca.2019.01.031>

Chen, F., Hegner, E., & Todt, W. (2000). Zircon ages and Nd isotopic and chemical compositions of orthogneisses from the Black Forest, Germany: Evidence for a Cambrian magmatic arc. *International Journal of Earth Sciences*, 88(4), 791–802. <https://doi.org/10.1007/s005310050306>

Cheng, Z., Zhang, Z., Hou, T., Santosh, M., Chen, L., Ke, S., & Xu, L. (2017). Decoupling of Mg-C and Sr-Nd-O isotopes traces the role of recycled carbon in magnesio-carbonatites from the Tarim large igneous province. *Geochimica et Cosmochimica Acta*, 202, 159–178. <https://doi.org/10.1016/j.gca.2016.12.036>

Cheng, Z., Zhang, Z., Xie, Q., Hou, T., & Ke, S. (2018). Subducted slab-plume interaction traced by magnesium isotopes in the northern margin of the Tarim large igneous province. *Earth and Planetary Science Letters*, 489, 100–110. <https://doi.org/10.1016/j.epsl.2018.02.039>

Dai, L. Q., Zhao, Z. F., Zheng, Y. F., An, Y. J., & Zheng, F. (2017). Geochemical distinction between carbonate and silicate metasomatism in generating the mantle sources of alkali basalts. *Journal of Petrology*, 58(5), 863–884. <https://doi.org/10.1093/petrology/egx038>

Dai, L.-Q., Zheng, F., Zhao, Z.-F., & Zheng, Y.-F. (2018). Geochemical insights into the lithology of mantle sources for Cenozoic alkali basalts in West Qinling, China. *Lithos*, 302–303, 86–98. <https://doi.org/10.1016/j.lithos.2017.12.013>

Dasgupta, R., & Hirschmann, M. M. (2010). The deep carbon cycle and melting in Earth's interior. *Earth and Planetary Science Letters*, 298(1–2), 1–13. <https://doi.org/10.1016/j.epsl.2010.06.039>

Dasgupta, R., Hirschmann, M. M., & Smith, N. D. (2007). Partial melting experiments of peridotite + CO₂ at 3 GPa and Genesis of alkalic ocean island basalts. *Journal of Petrology*, 48(11), 2093–2124. <https://doi.org/10.1093/petrology/egm053>

Dasgupta, R., Mallik, A., Tsuno, K., Withers, A. C., Hirth, G., & Hirschmann, M. M. (2013). Carbon-dioxide-rich silicate melt in the Earth's upper mantle. *Nature*, 493(7431), 211–215. <https://doi.org/10.1038/nature11731>

Deng, Y., & Tesauro, M. (2016). Lithospheric strength variations in Mainland China: Tectonic implications. *Tectonics*, 35(10), 2313–2333. <https://doi.org/10.1002/2016TC004272>

Dong, Y. P., Zhang, G. W., Neubauer, F., Liu, X. M., Genser, J., & Hauzenberger, C. (2011). Tectonic evolution of the Qinling Orogen, China: Review and synthesis. *Journal of Asian Earth Sciences*, 41(3), 213–237. <https://doi.org/10.1016/j.jseae.2011.03.002>

Fantle, M. S., & Tipper, E. T. (2014). Calcium isotopes in the global biogeochemical Ca cycle: Implications for development of a Ca isotope proxy. *Earth-Science Reviews*, 129, 148–177. <https://doi.org/10.1016/j.earscirev.2013.10.004>

Foley, S. F., Yaxley, G. M., Rosenthal, A., Buhre, S., Kiseeva, E. S., Rapp, R. P., & Jacob, D. E. (2009). The composition of near-solidus melts of peridotite in the presence of CO₂ and H₂O between 40 and 60 kbar. *Lithos*, 112(Supplement 1), 274–283. <https://doi.org/10.1016/j.lithos.2009.03.020>

Hammouda, T. (2003). High-pressure melting of carbonated eclogite and experimental constraints on carbon recycling and storage in the mantle. *Earth and Planetary Science Letters*, 214(1–2), 357–368. [https://doi.org/10.1016/S0012-821X\(03\)00361-3](https://doi.org/10.1016/S0012-821X(03)00361-3)

Huang, S., Farkas, J., & Jacobsen, S. B. (2011). Stable calcium isotopic compositions of Hawaiian shield lavas: Evidence for recycling of ancient marine carbonates into the mantle. *Geochimica et Cosmochimica Acta*, 75(17), 4987–4997. <https://doi.org/10.1016/j.gca.2011.06.010>

Ionov, D. A., Qi, Y.-H., Kang, J.-T., Golovin, A. V., Oleinikov, O. B., Zheng, W., et al. (2019). Calcium isotopic signatures of carbonatite and silicate metasomatism, melt percolation and crustal recycling in the lithospheric mantle. *Geochimica et Cosmochimica Acta*, 248, 1–13. <https://doi.org/10.1016/j.gca.2018.12.023>

Kang, J. T., Ionov, D. A., Liu, F., Zhang, C. L., Golovin, A. V., Qin, L. P., et al. (2017). Calcium isotopic fractionation in mantle peridotites by melting and metasomatism and Ca isotope composition of the bulk silicate Earth. *Earth and Planetary Science Letters*, 474, 128–137. <https://doi.org/10.1016/j.epsl.2017.05.035>

Kang, J. T., Ionov, D. A., Zhu, H. L., Liu, F., Zhang, Z. F., Liu, Z., & Huang, F. (2019). Calcium isotope sources and fractionation during melt-rock interaction in the lithospheric mantle: Evidence from pyroxenites, wehrlites, and eclogites. *Chemical Geology*, 524, 272–282. <https://doi.org/10.1016/j.chemgeo.2019.06.010>

Kiseeva, E. S., Yaxley, G. M., Hermann, J., Litasov, K. D., Rosenthal, A., & Kamenetsky, V. S. (2012). An experimental study of carbonated eclogite at 3–5–5.5 GPa—Implications for silicate and carbonatite metasomatism in the cratonic mantle. *Journal of Petrology*, 53(4), 727–759. <https://doi.org/10.1093/petrology/egr078>

Lai, S. C., Qin, J. F., & Khan, J. (2014). The carbonated source region of Cenozoic mafic and ultra-mafic lavas from Western Qinling: Implications for eastern mantle extrusion in the northeastern margin of the Tibetan Plateau. *Gondwana Research*, 25(4), 1501–1516. <https://doi.org/10.1016/j.gr.2013.05.019>

Li, S.-G., Yang, W., Ke, S., Meng, X., Tian, H., Xu, L., et al. (2017). Deep carbon cycles constrained by a large-scale mantle Mg isotope anomaly in eastern China. *National Science Review*, 4(1), 111–120. <https://doi.org/10.1093/nsr/nww070>

Li, W. Y., Teng, F. Z., Halama, R., Keller, J., & Klaudivius, J. (2016). Magnesium isotope fractionation during carbonatite magmatism at Oldoinyo Lengai, Tanzania. *Earth and Planetary Science Letters*, 444, 26–33. <https://doi.org/10.1016/j.epsl.2016.03.034>

Li, X. H., Liu, D. Y., Sun, M., Li, W. X., Liang, X. R., & Liu, Y. (2004). Precise Sm-Nd and U-Pb isotopic dating of the supergiant Shizhuyuan polymetallic deposit and its host granite, SE China. *Geological Magazine*, 141(2), 225–231. <https://doi.org/10.1017/s0016756803008823>

Li, X. H., Zhou, H. W., Chung, S. L., Lo, C. H., Wei, G. J., Liu, Y., & Lee, C. Y. (2002). Geochemical and Sr-Nd isotopic characteristics of late paleogene ultrapotassic magmatism in southeastern Tibet. *International Geology Review*, 44(6), 559–574. <https://doi.org/10.2747/0020-6814.44.6.559>

Ling, M. X., Liu, Y.-L., Williams, I. S., Teng, F.-Z., Yang, X.-Y., Ding, X., et al. (2013). Formation of the world's largest REE deposit through protracted fluxing of carbonatite by subduction-derived fluids. *Scientific Reports*, 3(1), 1776. <https://doi.org/10.1038/srep01776>

Liu, D., Zhao, Z., Niu, Y., Zhu, D., & Li, X.-H. (2018). Perovskite U-Pb and Sr-Nd isotopic perspectives on melilitite magmatism and outward growth of the Tibetan Plateau. *Geology*, 46(12), 1027–1030. <https://doi.org/10.1130/g45329.1>

Liu, S.-A., Qu, Y.-R., Wang, Z.-Z., Li, M.-L., Yang, C., & Li, S.-G. (2022). The fate of subducting carbon tracked by Mg and Zn isotopes: A review and new perspectives. *Earth-Science Reviews*, 228, 104010. <https://doi.org/10.1016/j.earscirev.2022.104010>

- Longhi, J. (1995). Liquidus equilibria of some primary lunar and terrestrial melts in the garnet stability field. *Geochimica et Cosmochimica Acta*, 59(11), 2375–2386. [https://doi.org/10.1016/0016-7037\(95\)00111-c](https://doi.org/10.1016/0016-7037(95)00111-c)
- Luth, R. W. (2014). Volatiles in Earth's mantle. In H. D. H. K. Turekian (Ed.), *Treatise on geochemistry* (2nd ed., pp. 355–391). Elsevier. <https://doi.org/10.1016/B978-0-08-095975-7.00207-2>
- Mallik, A., & Dasgupta, R. (2013). Reactive infiltration of MORB-eclogite-derived carbonated silicate melt into fertile peridotite at 3 GPa and Genesis of alkalic magmas. *Journal of Petrology*, 54(11), 2267–2300. <https://doi.org/10.1093/ptrology/egt047>
- Mallik, A., & Dasgupta, R. (2014). Effect of variable CO₂ on eclogite-derived andesite and lherzolite reaction at 3 Gpa-Implications for mantle source characteristics of alkalic ocean island basalts. *Geochemistry, Geophysics, Geosystems*, 15(4), 1533–1557. <https://doi.org/10.1002/2014GC005251>
- Panina, L. I., & Motorina, I. V. (2008). Liquid immiscibility in deep-seated magmas and the generation of carbonatite melts. *Geochemistry International*, 46(5), 448–464. <https://doi.org/10.1134/S0016702908050029>
- Pearson, D. G., Canil, D., & Shirey, S. B. (2014). Mantle samples included in volcanic rocks: Xenoliths and diamonds. In H. D. H. K. Turekian (Ed.), *Treatise on geochemistry* (2nd ed., pp. 169–253). Elsevier. <https://doi.org/10.1016/B978-0-08-095975-7.00216-3>
- Schauble, E. A. (2011). First-principles estimates of equilibrium magnesium isotope fractionation in silicate, oxide, carbonate and hexa-aqua-magnesium(2+) crystals. *Geochimica et Cosmochimica Acta*, 75(3), 844–869. <https://doi.org/10.1016/j.gca.2010.09.044>
- Shields, G., & Veizer, J. (2002). Precambrian marine carbonate isotope database: Version 1.1. *Geochemistry, Geophysics, Geosystems*, 3(6), 1 of 12–12 of 12. <https://doi.org/10.1029/2001gc000266>
- Shirey, S. B., Smit, K. V., Pearson, D. G., Walter, M. J., Aulbach, S., Brenker, F. E., et al. (2019). Diamonds and the mantle geodynamics of carbon: Deep mantle carbon evolution from the diamond record. In B. N. Orcutt, I. Daniel, & R. Dasgupta (Eds.), *Deep carbon: Past to present* (pp. 89–128). Cambridge University Press.
- Simon, J. I. (2022). Calcium isotope constraints on recycled carbonates in subduction-related magmas. In *Isotopic constraints on earth system processes* (pp. 43–56). <https://doi.org/10.1002/9781119595007.ch3>
- Stoppa, F., & Schiavizza, M. (2013). An overview of monogenetic carbonatitic magmatism from Uganda, Italy, China and Spain: Volcanologic and geochemical features. *Journal of South American Earth Sciences*, 41, 140–159. <https://doi.org/10.1016/j.jsames.2012.10.004>
- Su, B. X., Hu, Y., Teng, F. Z., Xiao, Y., Zhang, H. F., Sun, Y., et al. (2019). Light Mg isotopes in mantle-derived lavas caused by chromite crystallization, instead of carbonatite metasomatism. *Earth and Planetary Science Letters*, 522, 79–86. <https://doi.org/10.1016/j.epsl.2019.06.016>
- Su, B. X., Zhang, H. F., Sakyi, P. A., Ying, J. F., Tang, Y. J., Yang, Y. H., et al. (2010). Compositionally stratified lithosphere and carbonatite metasomatism recorded in mantle xenoliths from the Western Qinling (Central China). *Lithos*, 116(1–2), 111–128. <https://doi.org/10.1016/j.lithos.2010.01.004>
- Su, B. X., Zhang, H. F., Ying, J. F., Tang, Y. J., Hu, Y., & Santosh, M. (2012). Metasomatized lithospheric mantle beneath the Western Qinling, Central China: Insight into carbonatite melts in the mantle. *The Journal of Geology*, 120(6), 671–681. <https://doi.org/10.1086/667956>
- Sun, C., & Dasgupta, R. (2020). Thermobarometry of CO₂-rich, silica-undersaturated melts constrains cratonic lithosphere thinning through time in areas of kimberlitic magmatism. *Earth and Planetary Science Letters*, 550, 116549. <https://doi.org/10.1016/j.epsl.2020.116549>
- Sun, J., Zhu, X. K., Belshaw, N. S., Chen, W., Doroshkevich, A. G., Luo, W. J., et al. (2021). Ca isotope systematics of carbonatites: Insights into carbonatite source and evolution. *Geochemical Perspectives Letters*, 17, 11–15. <https://doi.org/10.7185/geochemlet.2107>
- Sun, S.-S., & McDonough, W. F. (1989). Chemical and isotopic systematics of oceanic basalts: Implications for mantle composition and processes. *Geological Society, London, Special Publications*, 42(1), 313–345. <https://doi.org/10.1144/gsl.sp.1989.042.01.19>
- Teng, F. Z. (2017). Magnesium isotope geochemistry. In F. Z. Teng, J. Watkins, & N. Dauphas (Eds.), *Non-traditional stable isotopes* (pp. 219–287). Mineralogical Society of America & Geochemical Society. <https://doi.org/10.2138/rmg.2017.82.7>
- Teng, F. Z., Li, W. Y., Rudnick, R. L., & Gardner, L. R. (2010). Contrasting lithium and magnesium isotope fractionation during continental weathering. *Earth and Planetary Science Letters*, 300(1–2), 63–71. <https://doi.org/10.1016/j.epsl.2010.09.036>
- Thomson, A. R., Walter, M. J., Kohn, S. C., & Brooker, R. A. (2016). Slab melting as a barrier to deep carbon subduction. *Nature*, 529(7584), 76–79. <https://doi.org/10.1038/nature16174>
- Tian, H.-C., Yang, W., Li, S.-G., Ke, S., & Chu, Z.-Y. (2016). Origin of low δ²⁶Mg basalts with EM-I component: Evidence for interaction between enriched lithosphere and carbonated asthenosphere. *Geochimica et Cosmochimica Acta*, 188, 93–105. <https://doi.org/10.1016/j.gca.2016.05.021>
- Wallace, P. J. (2005). Volatiles in subduction zone magmas: Concentrations and fluxes based on melt inclusion and volcanic gas data. *Journal of Volcanology and Geothermal Research*, 140(1–3), 217–240. <https://doi.org/10.1016/j.jvolgeores.2004.07.023>
- Wang, S.-J., & Li, S.-G. (2022). Magnesium isotope geochemistry of the carbonate-silicate system in subduction zones. *National Science Review*, 9(6), nwac036. <https://doi.org/10.1093/nsr/nwac036>
- Wang, S. J., Teng, F. Z., & Li, S. G. (2014). Tracing carbonate-silicate interaction during subduction using magnesium and oxygen isotopes. *Nature Communications*, 5(1), 6. <https://doi.org/10.1038/ncomms6328>
- Wang, W., Qin, T., Zhou, C., Huang, S. C., Wu, Z. Q., & Huang, F. (2017). Concentration effect on equilibrium fractionation of Mg-Ca isotopes in carbonate minerals: Insights from first-principles calculations. *Geochimica et Cosmochimica Acta*, 208, 185–197. <https://doi.org/10.1016/j.gca.2017.03.023>
- Wang, W., Zhou, C., Qin, T., Kang, J.-T., Huang, S. C., Wu, Z. Q., & Huang, F. (2017). Effect of Ca content on equilibrium Ca isotope fractionation between orthopyroxene and clinopyroxene. *Geochimica et Cosmochimica Acta*, 219, 44–56. <https://doi.org/10.1016/j.gca.2017.09.022>
- Wang, X.-J., Chen, L.-H., Hanyu, T., Zhong, Y., Shi, J.-H., Liu, X.-W., et al. (2021). Magnesium isotopic fractionation during basalt differentiation as recorded by evolved magmas. *Earth and Planetary Science Letters*, 565, 116954. <https://doi.org/10.1016/j.epsl.2021.116954>
- Wimpenny, J., Gislason, S. R., James, R. H., Gannoun, A., Pogge Von Strandmann, P. A. E., & Burton, K. W. (2010). The behaviour of Li and Mg isotopes during primary phase dissolution and secondary mineral formation in basalt. *Geochimica et Cosmochimica Acta*, 74(18), 5259–5279. <https://doi.org/10.1016/j.gca.2010.06.028>
- Workman, R. K., & Hart, S. R. (2005). Major and trace element composition of the depleted MORB mantle (DMM). *Earth and Planetary Science Letters*, 231(1–2), 53–72. <https://doi.org/10.1016/j.epsl.2004.12.005>
- Xiao, Y., Teng, F.-Z., Zhang, H.-F., & Yang, W. (2013). Large magnesium isotope fractionation in peridotite xenoliths from eastern North China craton: Product of melt–rock interaction. *Geochimica et Cosmochimica Acta*, 115, 241–261. <https://doi.org/10.1016/j.gca.2013.04.011>
- Yaxley, G. M., Green, D. H., & Kamenetsky, V. (1998). Carbonatite metasomatism in the southeastern Australian lithosphere. *Journal of Petrology*, 39(11–12), 1917–1930. <https://doi.org/10.1093/ptrology/39.11.1917>
- Yu, X. H., Zhao, Z. D., Mo, X. X., Zhou, S., Zhu, D. Q., & Wang, Y. L. (2006). 40Ar/39Ar dating for Cenozoic kamafugites from western Qinling in Gansu Province. *Chinese Science Bulletin*, 50(13), 1621–1627. <https://doi.org/10.1007/s11434-006-2010-7>
- Zhong, Y., Chen, L. H., Wang, X. J., Zhang, G. L., Xie, L. W., & Zeng, G. (2017). Magnesium isotopic variation of oceanic island basalts generated by partial melting and crustal recycling. *Earth and Planetary Science Letters*, 463, 127–135. <https://doi.org/10.1016/j.epsl.2017.01.040>

- Zhu, H., Liu, F., Li, X., An, Y., Nan, X., Du, L., et al. (2020). Significant $\delta^{44}/^{40}\text{Ca}$ variations between carbonate- and clay-rich marine sediments from the lesser antilles forearc and implications for mantle heterogeneity. *Geochimica et Cosmochimica Acta*, 276, 239–257. <https://doi.org/10.1016/j.gca.2020.02.033>
- Zhu, H., Liu, F., Li, X., An, Y., Wang, G., & Zhang, Z. (2018). A “peak cut” procedure of column separation for calcium isotope measurement using the double spike technique and thermal ionization mass spectrometry (TIMS). *Journal of Analytical Atomic Spectrometry*, 33(4), 547–554. <https://doi.org/10.1039/C8JA00004B>
- Zhu, H. L., Zhang, Z. F., Wang, G. Q., Liu, Y. F., Liu, F., Li, X., & Sun, W. D. (2016). Calcium isotopic fractionation during ion-exchange column chemistry and Thermal Ionisation Mass Spectrometry (TIMS) determination. *Geostandards and Geoanalytical Research*, 40(2), 185–194. <https://doi.org/10.1111/j.1751-908X.2015.00360.x>

References From the Supporting Information

- Young, E. D., & Galy, A. (2004). The isotope geochemistry and cosmochemistry of magnesium. *Reviews in Mineralogy and Geochemistry*, 55(1), 197–230. <https://doi.org/10.2138/gsrmg.55.1.197>